

# An experimental data base for the development, calibration and verification of constitutive models for sand with focus to cyclic loading.

## Part I: tests with monotonic loading and stress cycles

T. Wichtmann<sup>i)</sup> Th. Triantafyllidis<sup>ii)</sup>

---

**Abstract:** For numerical studies of geotechnical structures under earthquake loading, aiming to examine a possible failure due to liquefaction, using a sophisticated constitutive model for the soil is indispensable. Such model must adequately describe the material response to a cyclic loading under constant volume (undrained) conditions, amongst others the relaxation of effective stress (pore pressure accumulation) or the effective stress loops repeatedly passed through after a sufficiently large number of cycles (cyclic mobility, stress attractors). The soil behaviour under undrained cyclic loading is manifold, depending on the initial conditions (e.g. density, fabric, effective mean pressure, stress ratio) and the load characteristics (e.g. amplitude of the cycles, application of stress or strain cycles). In order to develop, calibrate and verify a constitutive model with focus to undrained cyclic loading, the data from high-quality laboratory tests comprising a variety of initial conditions and load characteristics are necessary. It is the purpose of these two companion papers to provide such data base collected for a fine sand. The data base consists of numerous undrained cyclic triaxial tests with stress or strain cycles applied to samples consolidated isotropically or anisotropically. Monotonic triaxial tests with drained or undrained conditions have been also performed. Furthermore, drained triaxial, oedometric or isotropic compression tests with several un- and reloading cycles are presented. Part I concentrates on the triaxial tests with monotonic loading or stress cycles. All test data presented herein will be available from the homepage of the first author. As an example of the examination of an existing constitutive model, the experimental data are compared to element test simulations using hypoplasticity with intergranular strain.

**Keywords:** data base, cyclic triaxial tests, monotonic triaxial tests, stress cycles, fine sand

---

### 1 Introduction

Numerical calculations of geotechnical structures (e.g. foundations, dams, slopes) on saturated non-cohesive soils subjected to earthquake loading demand a sophisticated constitutive model for the soil. Amongst others the model should reproduce the relaxation of effective stress (pore pressure accumulation) and describe all relevant stress attractors, i.e. the lens- or butterfly-shaped effective stress loops repeatedly passed through after a sufficiently large number of cycles. Several advanced constitutive models for non-cohesive soils have been developed during the last two decades, e.g. the hypoplastic model with intergranular strain [35, 51], the Sanisand elasto-plastic model [12, 13], or most recently the ISA model [16]. Crucial for the development of suitable constitutive equations and their calibration and verification is the availability of high-quality laboratory tests. These tests should have been performed with varying boundary conditions and control, so that the model can be checked for as many different cases as possible. Such close examination of the constitutive equations based on element tests creates confidence for an application of the model to different real problems.

However, most experimental studies with cyclic undrained tests in the literature are restricted to a certain type of

test, mostly triaxial tests with isotropic consolidation and stress cycles. For some frequently tested materials (e.g. Toyoura sand) there may be a suitable number of tests with different initial conditions and varying kind of control in the literature. However, collecting these results from a larger number of published studies may be laborious and uncomfortable - let alone the possible deviations of the results due to different sample preparation techniques, test devices and batches of the sand used by the different researchers. Therefore, there is a need for a comprehensive database with results from undrained cyclic laboratory tests with varying boundary conditions and load characteristics performed on a single sand. Such database has been collected for a fine sand at the IBF during the last few years.

Parts of the data have been already used to calibrate certain components of the high-cycle accumulation (HCA) model of Niemunis et al. [36]. The respective analysis is presented in [53, 55]. In the present companion papers, the experimental data is discussed in the context of conventional constitutive models (not high-cycle models), i.e. constitutive relations formulated in terms of stress and strain rates. The ISA model of Fuentes [16] has been developed based on parts of the data presented herein. This paper aims to make public the IBF experimental database also for other developers of constitutive models.

The data base can be used to improve existing models or establish new ones, delivering an appropriate prediction for various types of cyclic loading. The data base presented

---

<sup>i)</sup>Researcher, Institute of Soil Mechanics and Rock Mechanics (IBF), Karlsruhe Institute of Technology (KIT), Germany (corresponding author). Email: torsten.wichtmann@kit.edu

<sup>ii)</sup>Professor and Director of the IBF, KIT, Germany

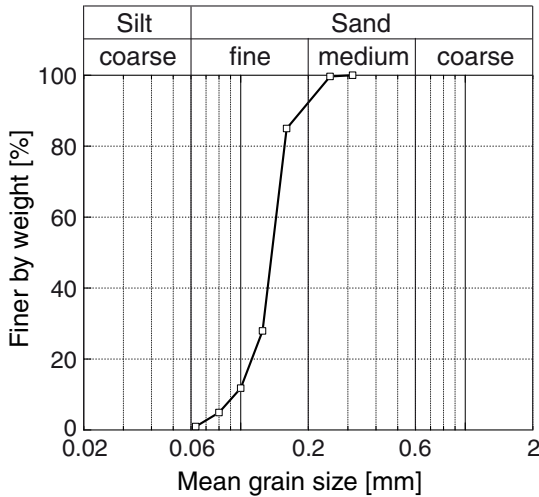


Fig. 1: Tested grain size distribution curve

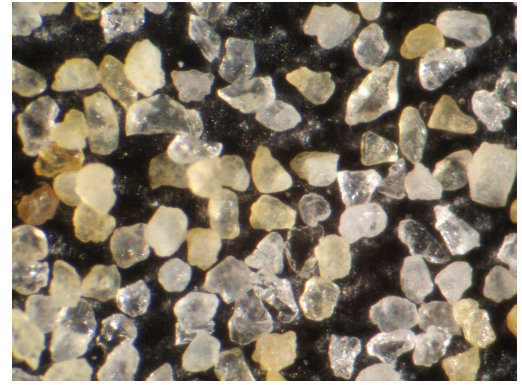


Fig. 2: Picture of grains of the tested sand taken with an optical microscope

in these two companion papers comprises the results from oedometric, isotropic compression and triaxial tests, with drained or undrained conditions and monotonic or cyclic loading. In the cyclic tests the samples were either consolidated isotropically or anisotropically and subjected to stress or strain cycles. The initial relative density was varied as well as the consolidation stress (mean pressure  $p_0$  and stress ratio  $\eta_0 = q_0/p_0$ ) and the stress or strain amplitude. Unless otherwise noted the tests have been performed on samples prepared by pluviating air-dried sand through a funnel. The relative density was varied by choosing different outlet diameters of the funnel.

All test data will be available from the homepage of the first author [52]. In case of the cyclic tests, the data provided at [52] contain both the measured data versus time and selected quantities versus the number of cycles.

The first part of the companion papers concentrates on the tests with monotonic loading and those performed with stress cycles. The second part reports on the cyclic tests with strain cycles and those conducted with a combined monotonic and cyclic loading.

In order to give an example for the examination of an existing constitutive model, some of the laboratory experiments have been recalculated using the element test program *Incremental Driver* of Niemunis [34] and hypoplasticity with intergranular strain [35, 51] as the constitutive model (see equations in Appendix A). The model prediction is compared to the experimental results.

## 2 Test material

The test material "Karlsruhe fine sand" has almost no fines content, a mean grain size  $d_{50} = 0.14$  mm and a uniformity coefficient  $C_u = d_{60}/d_{10} = 1.5$ . The grain size distribution curve is given in Figure 1. The minimum and maximum void ratios  $e_{\min} = 0.677$  and  $e_{\max} = 1.054$  were determined from standard tests (at mean pressure  $p = 0$ ) according to DIN 18126 [1]. Most of the grains have a subangular shape (see Figure 2).

## 3 Tests with monotonic loading

### 3.1 Oedometric tests

12 oedometric compression tests on dry samples with different initial relative densities  $0.04 \leq I_{D0} \leq 0.88$  with  $I_{D0} = (e_{\max} - e_0)/(e_{\max} - e_{\min})$  have been performed. The testing program is given in Table 1. The tests on loose and dense samples were used to calibrate the hypoplastic parameters  $h_s$ ,  $n$  and  $\beta$  (see Table 2). A relatively large sample size (diameter  $d = 150$  mm, height  $h = 30$  mm) has been used, because test series in the past, performed at IBF on samples with different geometries, had shown a considerable underestimation of oedometric stiffness for smaller samples ( $d = 100$  mm,  $h = 18$  mm), due to the larger influence of a thin zone at the top of the sample which is loosened during the sample preparation process. Due to the larger sample diameter and limitations of the loading device, the maximum applicable axial stress was restricted to  $\sigma_1 \approx 400$  kPa in the present test series. In the tests the axial stress was increased to  $\sigma_1 = 400$  kPa, followed by an unloading to  $\sigma_1 = 0$  and a reloading to  $\sigma_1 = 400$  kPa. The curves of void ratio  $e$  versus axial stress  $\sigma_1$  measured in the four tests with the lowest or highest initial relative densities, respectively, are provided in Figure 3a,b. Furthermore, the curves  $e(\sigma_1)$  from tests with other densities are given in Figure 6 of the companion paper [56]. Figure 3c presents the axial strain  $\varepsilon_1$  at the maximum stress  $\sigma_1 = 400$  kPa after first loading as a function of initial relative density  $I_{D0}$ . The diagram confirms the well-known increase of the compressibility with decreasing initial density.

The compression curves  $e(\sigma_1)$  during first loading obtained from simulations with hypoplasticity using the set of parameters given in Table 2 have been added as black solid curves in Figure 3. The intergranular strain has been assumed as initially fully mobilized in the vertical direction ( $h_{11} = -R$ ) which can be justified by the vertical sedimentation direction. The simulations were started at  $\sigma_1 = 1$  kPa. Since the four oedometric tests shown in Figure 3 have been used to calibrate the hypoplastic parameters given in Table 2, the simulations show a good agreement with the experimental data. Simulations of oedometric tests with un- and reloading cycles are further discussed in [56].

### 3.2 Drained triaxial tests

Unless otherwise noted all samples in the monotonic or cyclic triaxial tests presented in these two companion papers had a diameter of  $d \approx 100$  mm and a height of  $h \approx$

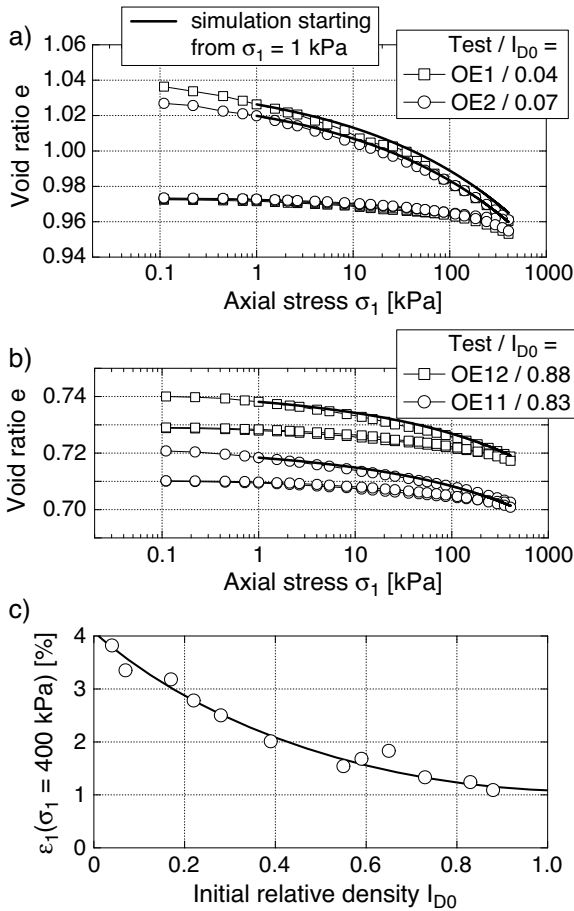


Fig. 3: a,b) Void ratio reduction  $e(\sigma_1)$  in oedometric tests on loose or dense samples; c) Axial strain  $\varepsilon_1$  at maximum load  $\sigma_1 = 400$  kPa after first loading as a function of initial relative density.

Test No.	$e_0$ [-]	$I_{D0}$ [-]
OE1	1.039	0.04
OE2	1.029	0.07
OE3	0.990	0.17
OE4	0.971	0.22
OE5	0.946	0.28
OE6	0.908	0.39
OE7	0.846	0.55
OE8	0.833	0.59
OE9	0.808	0.65
OE10	0.777	0.73
OE11	0.740	0.83
OE12	0.721	0.88

Table 1: Program of oedometric compression tests. Void ratios  $e_0$  and relative densities  $I_{D0}$  measured at axial stress  $\sigma_1 = 0$

100 mm. Smear end plates were used to minimize end frictional effects.

In the 25 drained monotonic triaxial compression tests, samples prepared to different relative densities in the range  $0.15 \leq I_{D0} \leq 0.95$  have been tested (see the testing program in Table 3). The samples were consolidated isotropically. For each of the five groups of densities, five different effective confining pressures  $\sigma'_3 = p_0 = 50, 100, 200, 300$  or  $400$  kPa have been chosen. The initial void ratios  $e_0$  and relative densities  $I_{D0}$  specified in Table 3 were measured at the initial pressure  $p_0$  of a test. The shearing was applied with a displacement rate of  $0.1$  mm/min in the axial direction.

Figure 4 presents the measured curves of deviatoric stress  $q$  and volumetric strain  $\varepsilon_v$  versus axial strain  $\varepsilon_1$  for loose, medium dense and dense samples. The well-known increase of peak deviatoric stress and dilatancy with increasing density is obvious in Figure 4. Furthermore, the dilatancy is stronger for the lower confining pressures. The peak friction angles  $\varphi_P$  derived from all drained monotonic triaxial tests have been collected in Figure 5. The exponential increase of  $\varphi_P$  with increasing initial relative density can be described by:

$$\varphi_P = 33.1^\circ \cdot \exp(0.293 \cdot I_{D0}^{1.76}) \quad (1)$$

(see the solid curve in Figure 5). The critical friction angle  $\varphi_c = \varphi_P(I_{D0} = 0) = 33.1^\circ$  has been determined from a loosely pluviated cone of sand, following the procedure explained e.g. in [22]. A slight decrease of  $\varphi_P$  with increasing pressure  $p_0$  can be concluded from Figure 5.

The values  $\varphi_r$  of friction angles at large strain ( $\varepsilon_1 = 25\%$  or the largest value applied in the test, respectively) are also provided in Figure 5. They are considerably lower than  $\varphi_P$ , but also show a slight density-dependence. This is probably due to the fact that the curves  $q(\varepsilon_1)$  provided in Figure 4 are still declining at large strains, i.e. a residual value is not fully reached.

The peak deviatoric stresses shown in Figure 4 were the basis for the calibration of the hypoplastic parameter  $\alpha$  given in Table 2. The hypoplastic simulations of these tests (and for all other triaxial tests with isotropic consolidation in this paper and in [56]) have been started from a state with isotropically fully mobilized intergranular strain, i.e.  $h_{ii} = -R/\sqrt{3}$ . This may be justified due to the preceding isotropic consolidation path. Simulations without a consideration of intergranular strain lead, however, to similar predicted curves. A satisfying reproduction of the stress-strain curves was achieved in the hypoplastic simulations (see dashed curves in the first row of diagrams in Figure 4) while the dilatancy at larger strains is underestimated for higher initial densities (second row of diagrams in Figure 4). The predicted dilatancy behaviour could be improved by a higher value of  $\alpha$ , but only on the cost of a significant overestimation of peak deviator stress. Note that such element test simulations do not consider localization of shear strain within the sample. The dilatancy in these shear zones is even larger than the globally measured one shown in Figure 4b,d,f.

Some additional drained monotonic triaxial tests were performed in order to study the influence of the displacement rate and the sample geometry. Dense samples were sheared with displacement rates of  $0.05, 0.1, 0.5$  and  $1.0$  mm/min in the axial direction. Beside the samples with  $d = h = 100$  mm, also higher ( $d = 100$  mm,  $h = 200$  mm) and

$\varphi_c$ [-]	$h_s$ [MPa]	$n$ [-]	$\alpha$ [-]	$\beta$ [-]	$e_{i0}$ [-]	$e_{c0}$ [-]	$e_{d0}$ [-]	$R$ [-]	$m_T$ [-]	$m_R$ [-]	$\beta_R$ [-]	$\chi$ [-]
33.1°	4000	0.27	0.14	2.5	1.212	1.054	0.677	10 <sup>-4</sup>	1.1	2.2	0.1	5.5

Table 2: Material parameters of hypoplasticity with intergranular strain for Karlsruhe fine sand

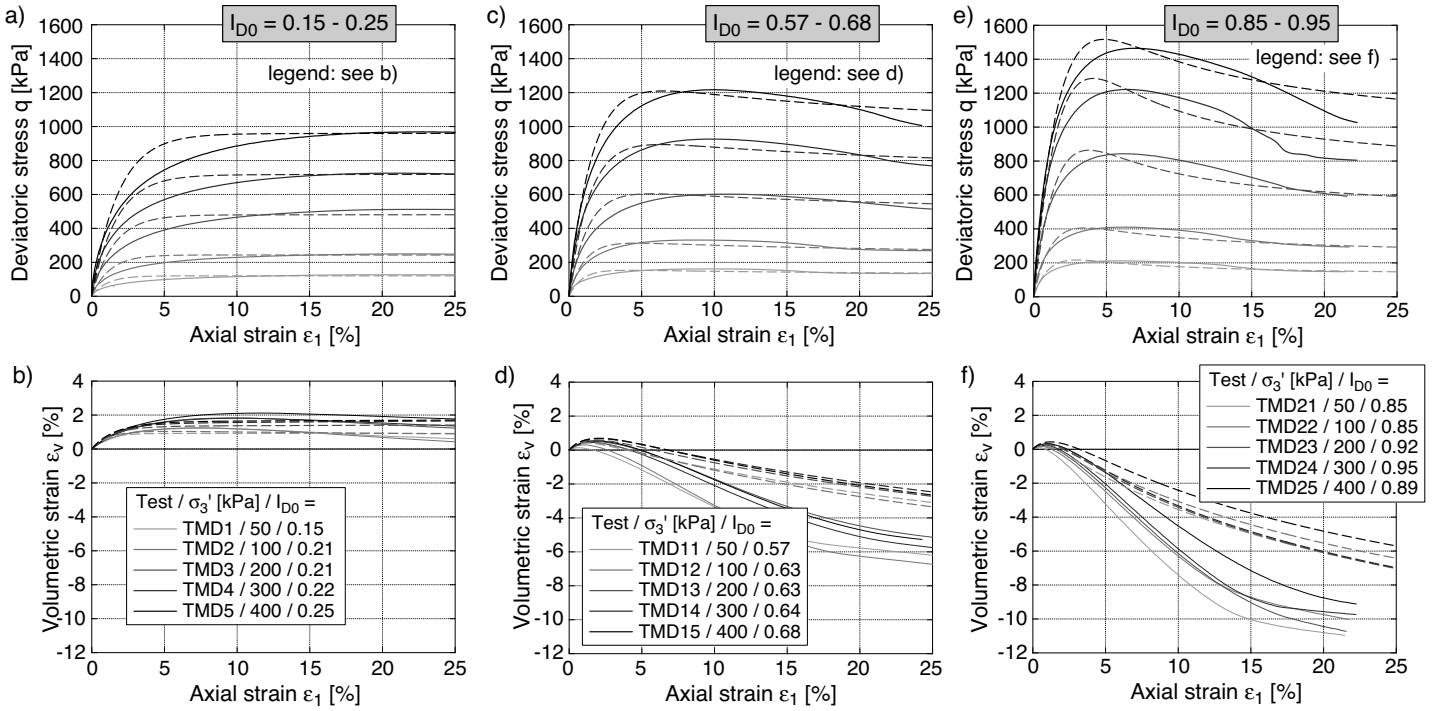


Fig. 4: Deviatoric stress  $q$  and volumetric strain  $\varepsilon_v$  versus axial strain  $\varepsilon_1$  in drained monotonic triaxial tests on a,b) loose, c,d) medium dense or e,f) dense samples. Solid curves = test results, dashed curves = simulations using hypoplasticity with intergranular strain

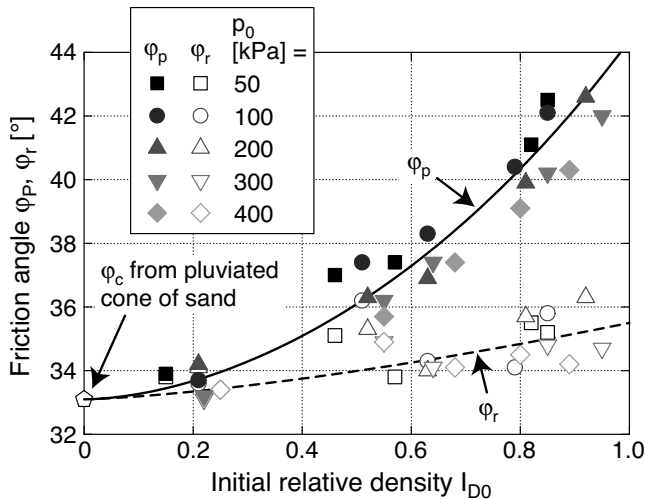


Fig. 5: Peak friction angle  $\varphi_P$  and residual friction angle  $\varphi_r$  (measured at  $\varepsilon_1 = 25\%$  or the last value applied in the test, respectively) derived from the drained monotonic triaxial tests as a function of initial relative density  $I_{D0}$

smaller ( $d = h = 50$  mm) samples were tested. In case of the samples with a height-to-diameter ratio equal to one, the number of lubrication layers applied at the top and bottom end plates has been varied. Beside the standard configuration with one layer of silicon grease and one rubber disk at each end, also stacks of two or four such layers have been tested. In the pioneer work of Bishop & Green [7] a decrease of the peak friction angle of about  $2^\circ$  had been observed in case of short samples ( $h/d = 1$ ) when the number of lubrication layers was increased from one to two or more. In Figure 6a the peak friction angle  $\varphi_P$  derived from all additional tests has been plotted versus initial relative density. As a measure of the stiffness during the initial phase of a test, the data of Young's modulus  $E_{50}$  is given in Figure 6b. The system compliance has been determined in tests on a steel dummy and considered in the evaluation of  $E_{50}$ . Neither the  $\varphi_P$  nor the  $E_{50}$  data in Figure 6 shows a significant influence of the displacement rate, the sample geometry or the number of lubrication layers. All further tests have thus been performed on samples with  $d = h = 100$  mm using a single lubrication layer at each end. Based on Figure 6, different displacement rates chosen in the various test series reported in the following, mainly due to differences in the applied test devices and their control and data acquisition systems, should be of minor importance regarding the observed material response.

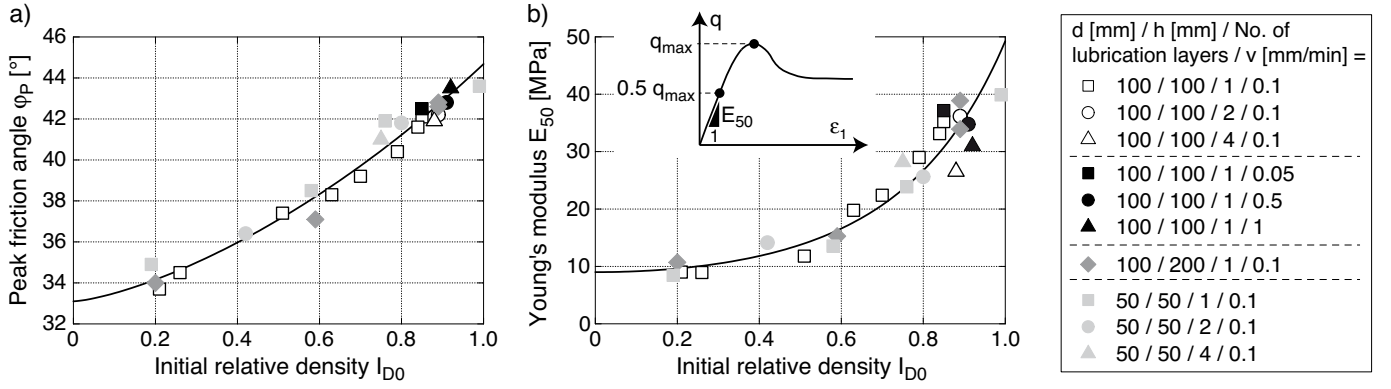


Fig. 6: a) Peak friction angle  $\varphi_P$  and b) Young's modulus  $E_{50}$  as a function of initial relative density derived from drained monotonic triaxial tests with different cylindrical sample geometries (diameter  $d$ , height  $h$ ), numbers of lubrication layers used at the end plates and displacement rates  $v$

Test No.	$e_0$ [-]	$I_{D0}$ [-]	$p_0$ [kPa]
TMD1	0.996	0.15	50
TMD2	0.975	0.21	100
TMD3	0.975	0.21	200
TMD4	0.970	0.22	300
TMD5	0.960	0.25	400
TMD6	0.880	0.46	50
TMD7	0.862	0.51	100
TMD8	0.859	0.52	200
TMD9	0.848	0.55	300
TMD10	0.847	0.55	400
TMD11	0.840	0.57	50
TMD12	0.819	0.63	100
TMD13	0.824	0.63	200
TMD14	0.822	0.64	300
TMD15	0.814	0.68	400
TMD16	0.743	0.82	50
TMD17	0.758	0.79	100
TMD18	0.748	0.81	200
TMD19	0.734	0.85	300
TMD20	0.753	0.80	400
TMD21	0.734	0.85	50
TMD22	0.735	0.85	100
TMD23	0.706	0.92	200
TMD24	0.697	0.95	300
TMD25	0.718	0.89	400

Table 3: Program of drained monotonic triaxial compression tests. Void ratios  $e_0$  and relative densities  $I_{D0}$  measured at initial mean pressure  $p_0$  prior to shearing

### 3.3 Undrained triaxial tests

#### 3.3.1 Test series 1

The undrained monotonic triaxial tests of the first series were performed with different initial pressures ( $100 \leq p_0 \leq 400$  kPa) and densities ( $0.24 \leq I_{D0} \leq 0.94$ ). Both, triaxial compression and extension tests have been conducted. The shearing was applied with a displacement rate of 0.02 mm/min. The testing program is summarized in Table 4. The measured stress-strain curves  $q(\varepsilon_1)$  and the effective stress paths in the  $p$ - $q$  plane are given in Figure 7. Figure 7a,b presents the data for different initial pressures and Figure 7c,d that for different densities. In accordance with the dilatancy behaviour observed in the drained tests, the samples with lower densities showed a larger relaxation of mean effective stress  $p$  during the initial phase of the tests (Figure 7c). Furthermore, the stress-strain relationships get steeper with increasing density (Figure 7d). The inclinations of the failure lines (FL) in the  $p$ - $q$  plane in triaxial compression ( $M_{c,FL}$ ) and extension ( $M_{e,FL}$ ) slightly increase with increasing initial density, while the corresponding values  $M_{c,PTL}$  and  $M_{e,PTL}$  of the phase transformation lines (PTL) decrease with  $I_{D0}$  (Figure 8). These dependencies can be described by the following equations [55]:

$$M_{c,FL} = 1.41 + 0.21(I_{D0})^{4.2} \quad (2)$$

$$M_{e,FL} = -0.95 - 0.041(I_{D0})^{4.2} \quad (3)$$

$$M_{c,PTL} = 1.03 + 0.65(1 - I_{D0})^{2.4} \quad (4)$$

$$M_{e,PTL} = -0.79 - 0.27(1 - I_{D0})^{1.9} \quad (5)$$

(see the solid or dashed curves in Figure 8, respectively).

The simulated stress-strain curves  $q(\varepsilon_1)$  (dashed curves in Figure 7b,d) show a quite satisfying congruence with the experimental data, while there are larger discrepancies in the  $p$ - $q$  effective stress paths (Figure 7a,c). The strong density-dependence of the dilatancy behaviour observed in the tests is not fully reflected by the applied constitutive model, i.e. the influence of density on the predicted effective stress paths is too weak. The overestimation of the relaxation of  $p$  during the initial phase of shearing (Figure 7a,c) is a well-known problem of the applied hypoplastic model [33] and is supported by the low value of  $m_T = 1.1$  (Table 2) which has been chosen as  $m_T = m_R/2$  with  $m_R$  calibrated from the cyclic test data (see Section 4.1).

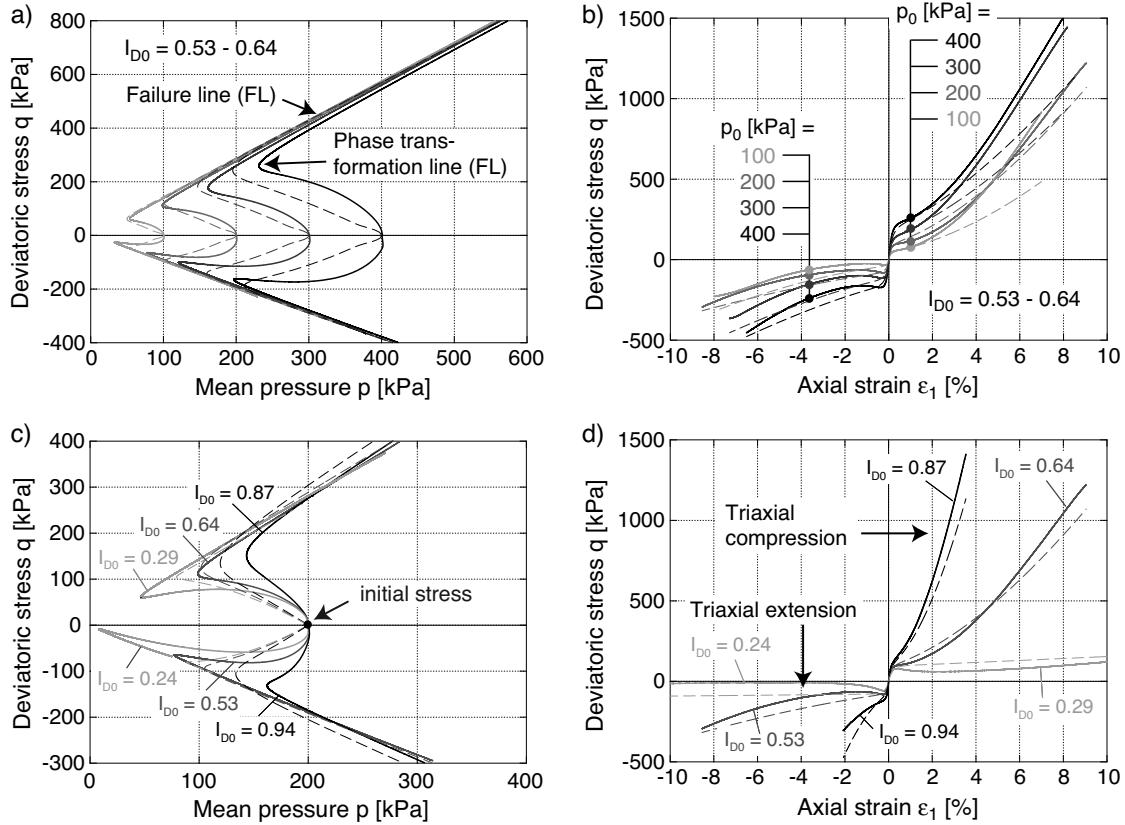


Fig. 7: Effective stress paths in the  $p$ - $q$ -plane and stress-strain relationships  $q(\epsilon_1)$  measured in undrained monotonic triaxial tests with different a,b) initial pressures and c,d) densities. Solid curves = test results, dashed curves = simulations using hypoplasticity with intergranular strain

Test	$e_0$ [-]	$I_{D0}$ [-]	$p_0$ [kPa]	Compression / Extension
TMU1	0.828	0.60	100	Comp
TMU2	0.814	0.64	200	Comp
TMU3	0.822	0.62	300	Comp
TMU4	0.819	0.62	400	Comp
TMU5	0.946	0.29	200	Comp
TMU6	0.728	0.87	200	Comp
TMU7	0.828	0.60	100	Ext
TMU8	0.853	0.53	200	Ext
TMU9	0.828	0.60	300	Ext
TMU10	0.827	0.60	400	Ext
TMU11	0.964	0.24	200	Ext
TMU12	0.698	0.94	200	Ext

Table 4: Program of undrained monotonic triaxial tests of series 1. Void ratios  $e_0$  and relative densities  $I_{D0}$  measured at initial mean pressure  $p_0$  prior to shearing

**3.3.2 Test series 2: Critical state from tests on samples prepared by moist tamping**

Most of the tests on medium dense and dense specimens presented in Section 3.3.1 had to be stopped at rather low strains  $\epsilon_1 < 10\%$  due to a decrease of pore water pressure below  $u = 0$  caused by dilatancy. A relatively low back pressure of  $u = 200$  kPa had been used in those tests. Since the pressure-dependent critical void ratio  $e_c(p)$  reached at large strains is an important component of most constitutive models, a second test series on relatively loose samples has been performed. Using the air pluviation technique it is hard to achieve initial relative densities in the triaxial tests below  $I_{D0} \approx 0.2$ . In order to reach even lower initial densities, most of the samples of this second test series have been prepared by moist tamping.

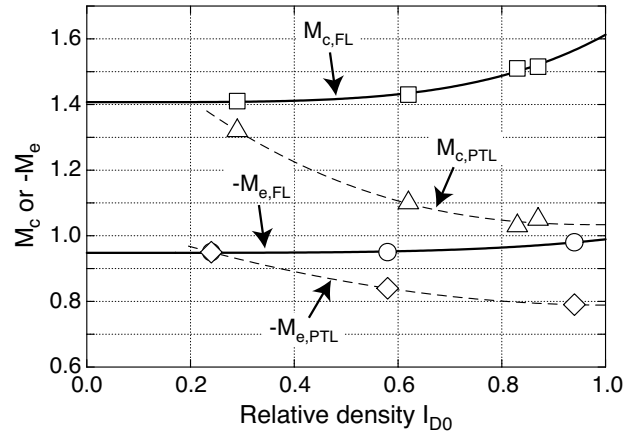


Fig. 8: Inclination  $M_c$  or  $M_e$  of the failure lines (FL) and the phase transformation lines (PTL) in triaxial compression or extension, respectively, as a function of relative density  $I_{D0}$

As discussed later in this section, the material response at low to intermediate strains is largely affected by the inherent fabric generated during the sample preparation process. It can be assumed, however, that the critical state

Test	$e_0$ [-]	$I_{D0}$ [-]	$p_0$ [kPa]	Preparation method
TMU-MT1	1.030	0.07	100	Moist tamping
TMU-MT2	0.941	0.30	100	Moist tamping
TMU-MT3	0.903	0.40	100	Moist tamping
TMU-MT4	1.026	0.07	300	Moist tamping
TMU-MT5	0.951	0.27	300	Moist tamping
TMU-MT6	0.905	0.39	300	Moist tamping
TMU-MT7	1.038	0.04	500	Moist tamping
TMU-MT8	0.942	0.30	500	Moist tamping
TMU-MT9	0.904	0.40	500	Moist tamping
TMU-AP1	0.928	0.33	100	Air pluviation
TMU-AP2	0.941	0.30	300	Air pluviation
TMU-AP3	0.932	0.32	500	Air pluviation

Table 5: Program of undrained monotonic triaxial tests of series 2 on loose samples prepared by either moist tamping or air pluviation. Void ratios  $e_0$  and relative densities  $I_{D0}$  measured at initial mean pressure  $p_0$  prior to shearing

does not depend on the initial fabric, because this fabric is presumably erased at large shear strains. Therefore, the critical void ratio  $e_c(p)$  derived from the tests on loose samples prepared by moist tamping is assumed applicable also for air-pluviated samples. In most tests of this second series strains of  $\varepsilon_1 > 25\%$  could be applied because the densities were relatively low and a relatively high back pressure (500 or 800 kPa) was chosen. A large number of tests (about 150) has been performed within this second series. Because a different sample preparation technique has been used, however, only some of these tests (Table 5) have been included in the data base discussed in this paper.

Figure 9 presents the stress-strain relationships and effective stress paths measured in the nine tests performed on samples prepared by moist tamping. The samples were consolidated at  $p_0 = 100, 300$  or  $500$  kPa and sheared with a displacement rate of  $0.1$  mm/min. In Figure 9 samples of similar initial density are grouped into one diagram. The very loose samples ( $0.04 \leq I_{D0} \leq 0.07$ , Figure 9a,b) show a purely contractive behaviour leading to a full liquefaction ( $p = q = 0$ ) or to a very low effective stress, respectively. In contrast, in case of the samples with higher initial density ( $0.27 \leq I_{D0} \leq 0.40$ , Figure 9c-f) the slight contractive tendency observed during the initial stage of the tests was followed by dilatancy at larger strains. Obviously, irrespectively of the initial effective stress, the final effective stress states at large strains ( $\varepsilon_1 \geq 25\%$ ) are similar for a given density. The data shown in Figure 9 look very similar to those of Verdugo & Ishihara [50] which are frequently used for the calibration of constitutive models in the literature. However, most of the initial pressures used in the present test series are lower than those applied in [50] ( $p_0 = 100, 1000, 2000$  and  $3000$  kPa have been used in [50]). The  $p_0$ -range examined in the present test series is thought to be of higher practical relevance for most in situ problems.

The void ratio  $e = e_0$  has been plotted versus the effective mean pressure  $p$  reached at large strain in Figure 10. Usually the data at  $\varepsilon_1 = 25\%$  has been used for that diagram. Some tests were stopped slightly before having reached  $\varepsilon_1 = 25\%$ , see e.g. Figure 9e. In that case the  $p$  values at the largest tested axial strain have been selected. In Figure 10, the initial states of the tests are marked by

the empty symbols while the states at  $\varepsilon_1 = 25\%$  are shown by the filled ones. Most samples showed an almost constant value of  $q$  or only a moderate increase of the deviatoric stress with continued shearing at that large strain (see the first row of diagrams in Figure 9). Therefore, the data at  $\varepsilon_1 \approx 25\%$  can be approximately assigned to a critical state. Figure 10 does not only contain the data from the tests listed in Table 5 but also the results from numerous similar tests with varying initial densities. Data from tests on air-pluviated samples (amongst others from the three tests TMU-AP1 - TMU-AP3 listed in Table 5) are also provided in Figure 10. An almost unique critical state line  $e_c(p)$  for samples prepared by either moist tamping or air pluviation can be concluded from Figure 10, at least in the range of void ratios tested with both samples preparation techniques. The relationship  $e_c(p)$  can be described by the equation of Bauer [5] (see dashed curve in Figure 10):

$$e_c = e_{c0} \cdot \exp[-(3p/h_s)^n] \quad (6)$$

with  $e_{c0} = 1.067$ ,  $h_s = 860$  MPa and  $n = 0.32$ .

Usually the hypoplastic parameters  $h_s$  and  $n$  are not calibrated from the critical state derived from a laborious triaxial test series as that presented in Figure 10, but estimated from the oedometric compression curve measured on loose samples (see Figure 3a). The parameters given in Table 2 have been also obtained from oedometric test data for loose sand. The prediction of Eq. (17) with the parameters  $e_{c0} = e_{\max} = 1.054$ ,  $h_s = 4000$  MPa and  $n = 0.27$  (Table 2) derived from the index or oedometric tests has been added as dot-dashed curve in Figure 10. It can be concluded that this estimated critical state line  $e_c(p)$  is not far away from the critical state derived from the undrained monotonic triaxial tests.

Figure 11 compares the states  $(e, p)$  measured at  $\varepsilon_1 = 25\%$  (or at the largest strain applied in the test, respectively) in the undrained and drained monotonic triaxial tests. The data from the drained tests on the loosest samples ( $I_{D0} = 0.15 - 0.25$ ) agree well with those from the undrained tests. With increasing density, however, the points  $(e, p)$  obtained from the drained tests are shifted towards lower void ratios, i.e. the deviation from the undrained test data increases. This is probably due to a larger localization of strain in the drained tests. Due to a more pronounced development of shear bands, a lower fraction of the sample volume is involved in shearing and thus in dilatancy, leading to lower values of average void ratio derived from the global volume change measurements. Furthermore, it should be kept in mind that most of the curves of volumetric strain  $\varepsilon_v(\varepsilon_1)$  from the drained tests provided in Figure 4 have not reached an asymptotic value at  $\varepsilon_1 = 25\%$  or at the largest strain applied in the test, respectively, yet. Further shearing would probably have led to a continued dilatancy of the sand, resulting in larger void ratios in Figure 11.

The comparison of the effective stress paths and stress-strain relationships of samples with similar density, prepared either by air pluviation or moist tamping, in Figure 9c,d reveals the large effect of initial fabric on the material response to undrained monotonic shearing. For initial densities in the range  $0.27 \leq I_{D0} \leq 0.33$ , the pluviated samples (tests TMU-AP1 - TMU-AP3 in Table 5) show a much larger relaxation of effective mean pressure  $p$  in the initial phase of a test than those constituted by moist tamping. In contrast to the tamped samples, the pluviated ones pass a

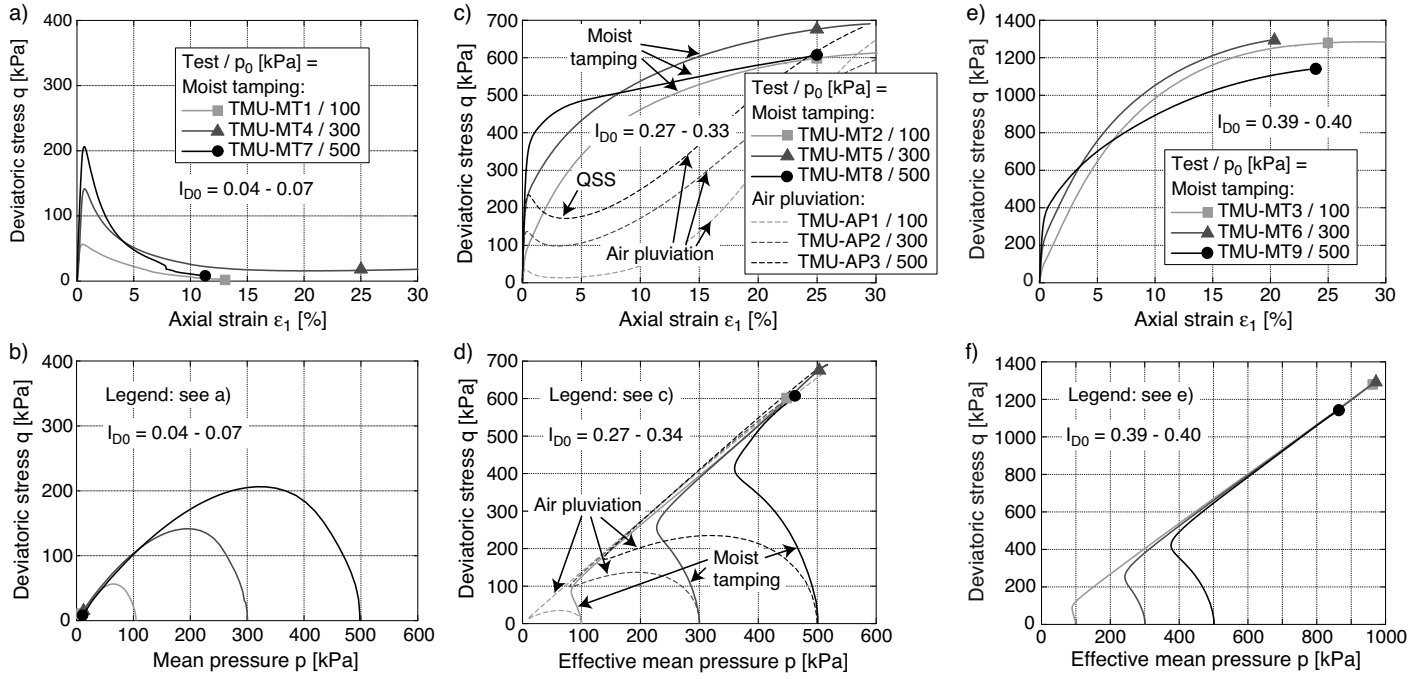


Fig. 9: Stress-strain relationships and effective stress paths in undrained monotonic triaxial tests performed on relatively loose samples prepared by either moist tamping or air pluviation. The state at large strains (approximately critical state) is marked by a symbol

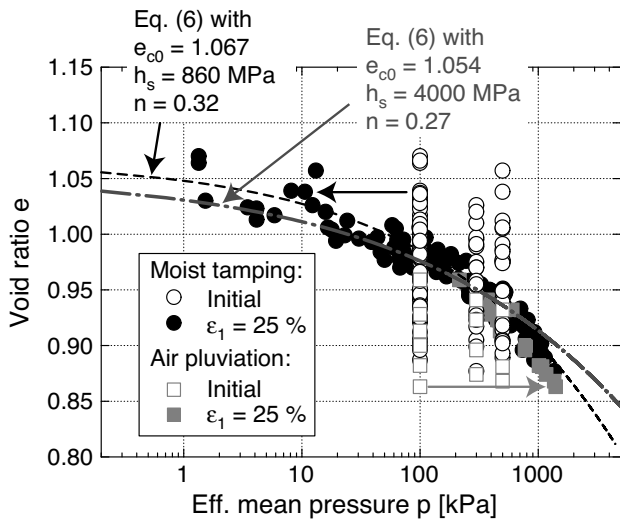


Fig. 10: State  $(e, p)$  at  $\epsilon_1 = 25\%$  (approximately critical state  $e_c(p)$ ) of samples prepared with different initial densities by either air pluviation or moist tamping and consolidated at different initial pressures ( $p_0 = 100, 300$  or  $500$  kPa)

quasi-steady state (QSS), i.e. a local minimum of the deviatoric stress at phase transformation. The samples prepared by both methods, however, reach a similar effective stress (critical state) at large strains (Figure 9d), which confirms the conclusion of a unique relationship  $e_c(p)$  from Figure 10.

In order to obtain a consistent set of data, all cyclic tests presented in the following (and also in the companion paper [56]) have been performed using the same sample preparation technique, namely air pluviation. The influence of fabric on the material response of Karlsruhe fine sand will be discussed in more detail in another paper.

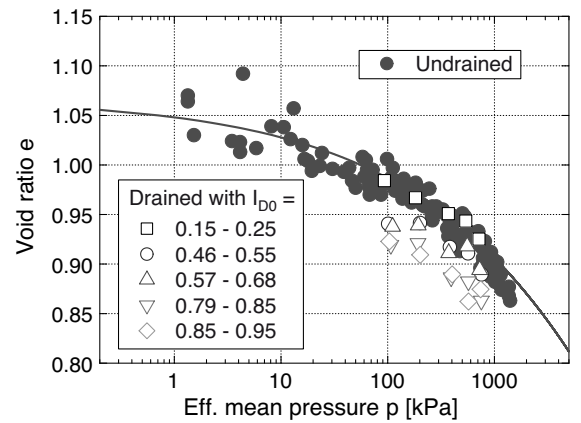


Fig. 11: Comparison of state  $(e, p)$  at  $\epsilon_1 = 25\%$  in undrained and drained monotonic tests

#### 4 Undrained tests with stress cycles

##### 4.1 Tests with isotropic consolidation

The cycles have been applied using a constant displacement rate of  $0.05$  mm/min. In order to test a certain stress amplitude  $q^{amp}$ , the loading direction was changed once the specified minimum or maximum values of deviatoric stress were reached (pseudo stress-control). Several tests with different initial densities ( $0.24 \leq I_{D0} \leq 0.87$ ), initial pressures ( $100 \leq p_0 \leq 300$  kPa) and amplitude-pressure ratios ( $0.15 \leq q^{amp}/p_0 \leq 0.50$ ) have been performed. The testing program is summarized in Table 6.

Some of the tests with isotropic consolidation stresses included in this data base have been primarily performed in order to calibrate the bulk modulus  $K$  of the "elastic" stiffness used in the HCA model [53]. For such a calibration, the application of a first drained cycle prior to the undrained cyclic loading is advantageous [53]. The drained

Test	$e_{0d}$	$I_{D0d}$	$e_0$	$I_{D0}$	$p_0$	$q^{ampl}$	$q^{ampl}/p_0$	1. drained cycle?	$N_{ini}$
	[-]	[-]	[-]	[-]	[kPa]	[kPa]	[-]		[-]
Loose									
TCUI1	-	-	0.952	0.27	200	30	0.15	no	72
TCUI2	0.962	0.24	0.961	0.25	100	15	0.15	yes	87
TCUI3	0.950	0.28	0.949	0.28	100	20	0.20	yes	15
TCUI4	0.963	0.24	0.961	0.25	100	25	0.25	yes	5
TCUI5	0.956	0.26	0.956	0.26	200	30	0.15	yes	86
TCUI6	0.964	0.24	0.964	0.24	300	45	0.15	yes	144
Medium dense									
TCUI7	-	-	0.800	0.67	200	60	0.30	no	11
TCUI8	0.822	0.62	0.821	0.62	100	20	0.20	yes	249
TCUI9	0.799	0.68	0.798	0.68	100	25	0.25	yes	100
TCUI10	0.826	0.60	0.825	0.61	100	30	0.30	yes	15
TCUI11	0.843	0.56	0.842	0.56	200	40	0.20	yes	146
TCUI12	0.814	0.64	0.813	0.64	200	50	0.25	yes	77
TCUI13	0.834	0.58	0.832	0.59	200	60	0.30	yes	15
TCUI14	0.847	0.55	0.846	0.55	300	60	0.20	yes	257
TCUI15	0.809	0.65	0.808	0.65	300	75	0.25	yes	110
TCUI16	0.817	0.63	0.816	0.63	300	90	0.30	yes	24
Dense									
TCUI17	-	-	0.726	0.87	200	60	0.30	no	185
TCUI18	0.760	0.78	0.759	0.78	100	30	0.30	yes	54
TCUI19	0.762	0.77	0.761	0.78	100	40	0.40	yes	15
TCUI20	0.757	0.79	0.755	0.79	100	50	0.50	yes	6
TCUI21	0.755	0.79	0.754	0.80	200	60	0.30	yes	61
TCUI22	0.745	0.82	0.744	0.82	300	90	0.30	yes	269

Table 6: Program of undrained cyclic triaxial tests with isotropic consolidation ( $\eta_0 = q_0/p_0 = 0$ ) and stress cycles. Void ratios  $e_0$  and relative densities  $I_{D0}$  are measured at initial mean pressure  $p_0$  prior to undrained cyclic shearing.  $e_{0d}$  and  $I_{D0d}$  are the values at  $p_0$  prior to the first drained cycle (if applied).  $N_{ini}$  is the number of cycles to initial liquefaction.

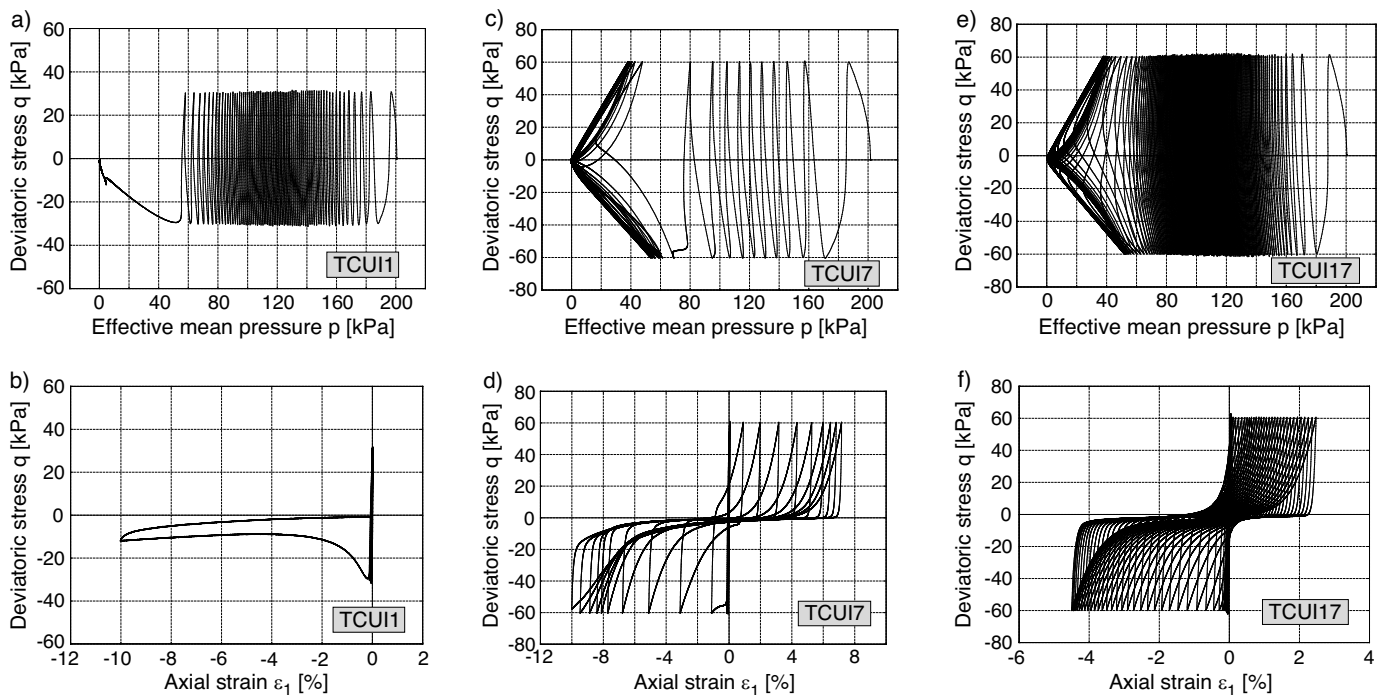


Fig. 12: Results of undrained cyclic tests with isotropic initial stresses and stress cycles, performed without a first drained cycle a,b) test TCUI1 ( $I_{D0} = 0.27$ ,  $q^{ampl} = 30$  kPa), c,d) test TCUI7 ( $I_{D0} = 0.67$ ,  $q^{ampl} = 60$  kPa), e,f) test TCUI17 ( $I_{D0} = 0.87$ ,  $q^{ampl} = 60$  kPa)

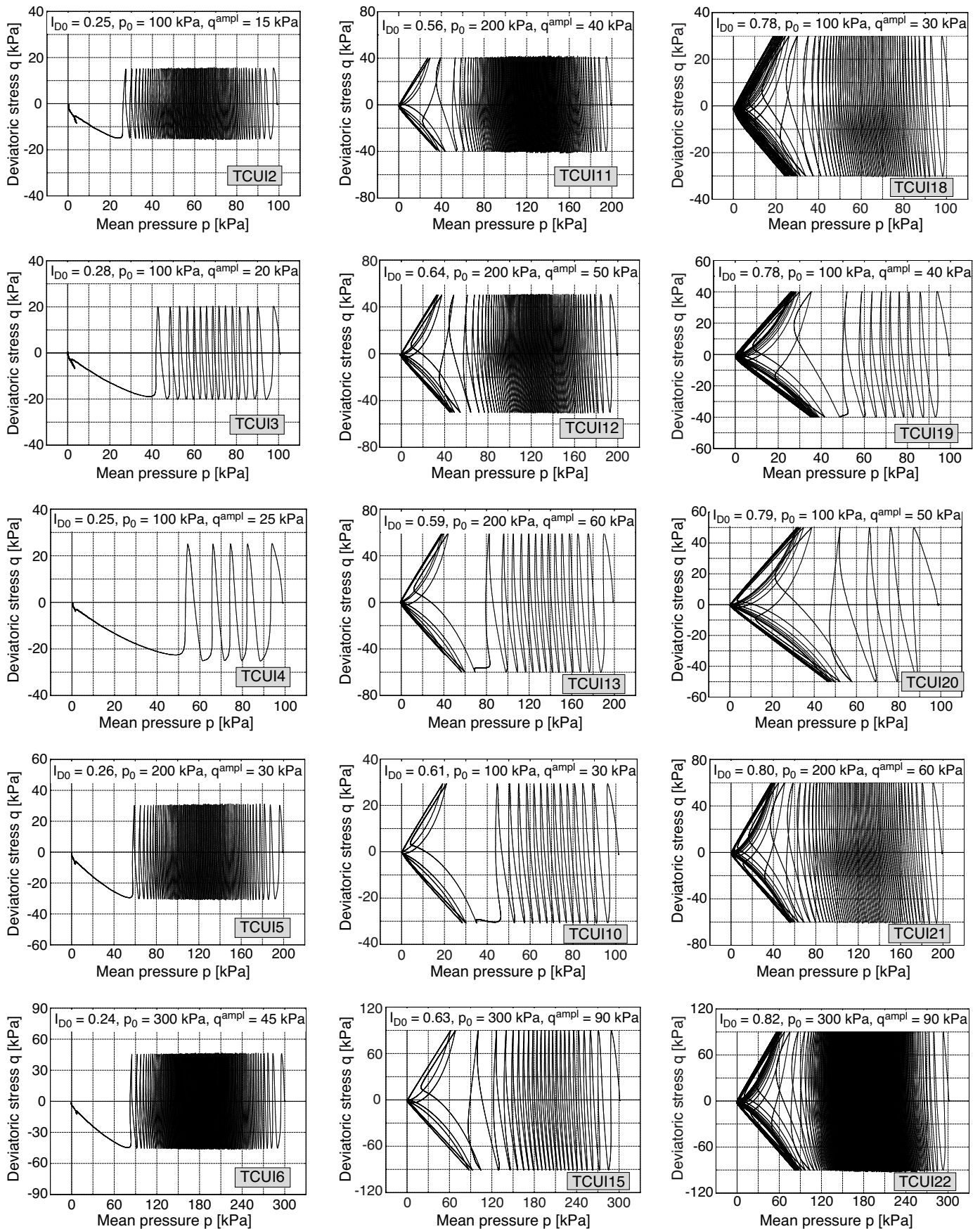


Fig. 13: Effective stress paths in undrained cyclic tests with isotropic initial stresses and stress cycles performed on loose specimens (left-hand side), medium dense specimens (middle) and dense specimens (right-hand side)

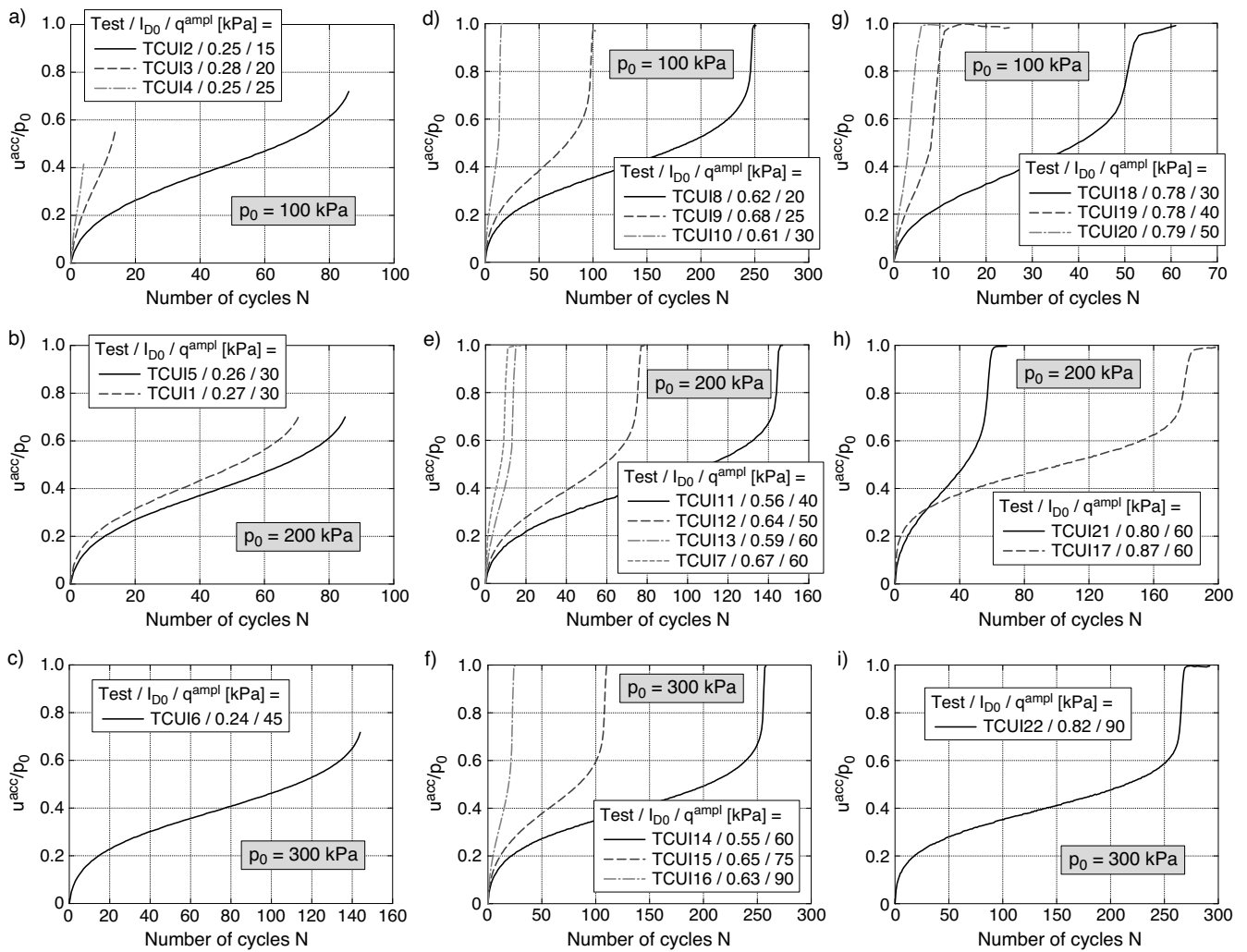


Fig. 14: Ratio of accumulated pore water pressure  $u^{acc}$  and initial mean effective stress  $p_0$  as a function of the number of cycles measured in undrained cyclic triaxial tests with different initial densities  $I_{D0}$ , initial pressures  $p_0$  and stress amplitudes  $q^{amp}$

cycle is applied with the same stress amplitude as the subsequent undrained cycles. In Table 6 it is indicated whether the tests have been performed with or without a drained first cycle. The initial void ratios and relative densities prior to the first drained cycle (if applied) are given as  $e_{0d}$  and  $I_{D0d}$  in Table 6. A comparison of the  $e_{0d}$  (before first cycle) and  $e_0$  (after first cycle) values in Table 6 reveals that the compaction caused by this first drained cycle is relatively small. Furthermore, the first drained cycle has only a moderate effect on the observed material response during the subsequent undrained cyclic loading. It represents a preloading and thus slightly decreases the rate of stress relaxation during the initial stage of the undrained cyclic test phase. The drained first cycle should be considered when recalculating these tests in order to check a constitutive model.

A typical result from a test on a loose sample ( $I_{D0} = 0.27$ , test TCUI1, without first drained cycle) is shown in Figure 12a,b. The diagrams present the effective stress path in the  $p$ - $q$  plane and the deviatoric stress versus axial strain. Large axial extension strains, fulfilling the failure criterion  $|\epsilon_1| = 10\%$  chosen for loose sand, developed when the effective stress path reached the failure line in the triaxial extension regime. A liquefaction, i.e. a relaxation of mean

effective stress to  $p = 0$  was reached only at the end of the test, after the axial strain had been reduced to  $\epsilon_1 = 0$ . Similar effective stress paths were measured in all tests on loose samples (TCUI2 - TCUI6), for different amplitude-pressure ratios ( $0.15 \leq q^{amp}/p_0 \leq 0.25$ ) and initial pressures ( $100 \leq p_0 \leq 300$  kPa), see the first column of diagrams in Figure 13.

A typical result of a test performed on a medium dense sample ( $I_{D0} = 0.67$ , test TCUI7) is provided in Figure 12c,d. When the effective stress path comes close to the failure line in the triaxial extension regime, it starts to follow a butterfly-shaped loop and the axial strain amplitude increases with each subsequent cycle. Such behaviour is known as "cyclic mobility". After the initial liquefaction (i.e.  $p = 0$  is reached for the first time) large axial strains can be applied without mobilizing any relevant shear resistance (i.e.  $q \approx 0$ , Figure 12d). The stress-strain hysteresses in Figure 12d show that the range of axial strain with almost zero mobilized shear resistance grows with increasing number of cycles. In case of the medium dense samples failure was also associated with an axial strain of  $|\epsilon_1| = 10\%$ . The effective stress paths measured in other tests on medium dense samples (TCUI10 - TCUI13 and TCUI15), with different values of  $p_0$  and  $q^{amp}/p_0$ , are given in the

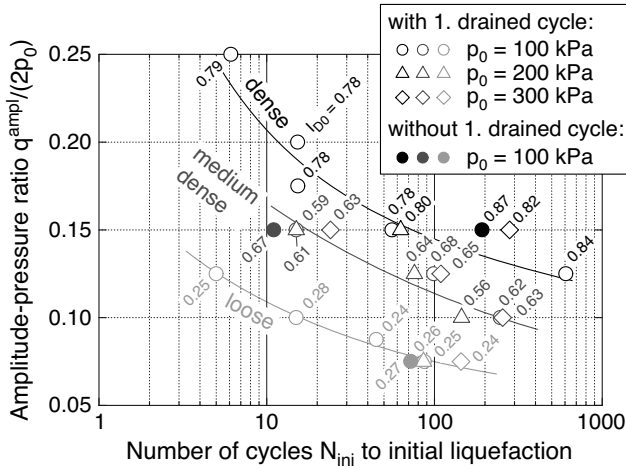


Fig. 15: Amplitude-pressure ratio versus number of cycles to initial liquefaction in dependence of initial relative density  $I_{D0}$  and consolidation pressure  $p_0$

middle column of diagrams in Figure 13. These stress paths look similar to that provided in Figure 12c.

In principle, the results for dense samples do not significantly differ from those obtained for medium dense sand (see a typical result from test TCUI17 with  $I_{D0} = 0.87$  in Figure 12e,f). Butterfly-shaped effective stress loops in the final stage of the test and a temporary liquefaction ( $p = 0$ ) during these cycles are observed also for the dense sample. However, the increase of the axial strain amplitude with the number of cycles after initial liquefaction takes place at a significantly lower rate than for the medium dense sample, i.e. much more cycles can be applied in the cyclic mobility phase until a certain failure criterion (here:  $|\varepsilon_1| = 4.5\%$ ) has been reached. More effective stress paths from tests on dense samples (TCUI18 - TCUI22) with varying consolidation stresses and stress amplitudes, looking similar to that in Figure 12e, are provided in the third column of diagrams in Figure 13.

The data in Figures 12 and 13 agrees well with numerous experimental studies on the liquefaction resistance of non-cohesive soils published in the literature. Similar effective stress paths from triaxial, torsional shear or simple shear tests have been presented e.g. in [14, 17–21, 24, 25, 28, 29, 31, 37, 38, 40, 44, 46–49, 54, 57, 59–63, 66, 67].

Figure 14 presents the ratio  $u^{acc}/p_0$  of accumulated pore water pressure and initial mean effective stress as a function of the number of cycles. The data is given up to the end of the last full cycle prior to failure (therefore the curves for loose samples end before  $u^{acc}/p_0 = 1$ ). For a given relative density and a certain initial pressure, the increase of the pore pressure accumulation rate with increasing stress amplitude is obvious in Figure 14. The number of cycles to initial liquefaction is provided in the last column of Table 6. Figure 15 shows the amplitude-pressure ratio  $q^{amp}/(2p_0)$  versus this number of cycles. The diagram contains the data of all undrained cyclic triaxial tests performed on isotropically consolidated samples. The well-known increase of the liquefaction resistance with increasing density of the samples is obvious in Figure 15. In case of medium dense and dense samples, for  $q^{amp}/(2p_0) = \text{constant}$ , an increase of the number of cycles to initial liquefaction with increasing consolidation pressure  $p_0$  can be concluded. The pres-

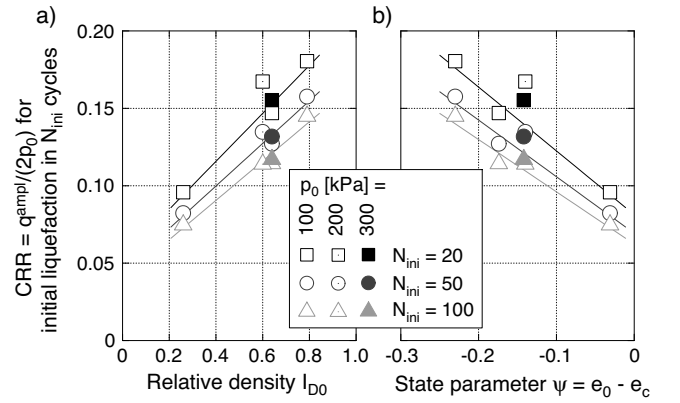


Fig. 16: Amplitude-pressure ratio causing initial liquefaction in a certain number of cycles  $N_{ini}$  as a function of a) relative density  $I_{D0}$  and b) state parameter  $\psi = e_0 - e_c(p_0)$

sure dependence is less pronounced for the loose samples. Furthermore, Figure 15 confirms that the liquefaction resistance is only moderately affected by the first drained cycle applied in some of the tests. For a given density, the data points from the tests with (empty symbols) or without (filled symbols) such cycle lie almost on the same curve.

The amplitude-pressure ratio  $CRR = q^{amp}/(2p_0)$  causing initial liquefaction in a certain number of cycles ( $N_{ini} = 20, 50$  or  $100$ ) has been evaluated based on Figure 15 and plotted versus relative density  $I_{D0}$  or state parameter  $\psi = e_0 - e_c(p_0)$  [6] in Figure 16. The state parameter  $\psi$  is increasingly employed in an analysis of the liquefaction resistance (e.g. [3, 4, 8–10, 15, 23, 42, 43]). It has been evaluated with critical void ratio  $e_c(p_0)$  calculated from Eq. (17). For the higher initial pressures  $p_0 = 200$  and  $300$  kPa only data for medium dense samples is included in Figure 16. In contrast to the medium dense sand, in case of the loose and dense samples only a single amplitude-pressure ratio has been tested at  $p_0 = 200$  and  $300$  kPa and thus the corresponding curves  $CRR(N_{ini})$  extrapolated from this single data point may not be reliable. An almost linear increase of the liquefaction resistance with increasing relative density and with decreasing state parameter  $\psi$  can be concluded from Figure 16. In the range of tested  $p_0$  values, no clear advantage of the analysis in terms of  $\psi$  over that with  $I_{D0}$  can be observed in Figure 16, since the scatter of data is even slightly larger in the  $CRR-\psi$  diagram. However, an analysis with  $\psi$  may be advantageous if a larger range of pressures, involving also significantly higher pressures, is considered.

The relatively low displacement rate in the cyclic tests (0.05 mm/min) has been chosen in order to accurately control the maximum and minimum deviatoric stresses. In order to check the influence of the loading rate, four additional cyclic tests with larger displacement rates  $v = 0.1$  or  $0.2$  mm/min have been performed on medium dense samples, using an isotropic initial stress with  $p_0 = 200$  kPa. Two different stress amplitudes were tested for each displacement rate. In agreement with the data from drained monotonic tests in Figure 6, the material response under undrained cyclic loading was found rather insensitive to the displacement rate. The  $q^{amp}/(2p_0)-N_{ini}$  diagram in Figure 17 reveals that the number of cycles to initial liquefaction is approximately independent of the loading rate. This is

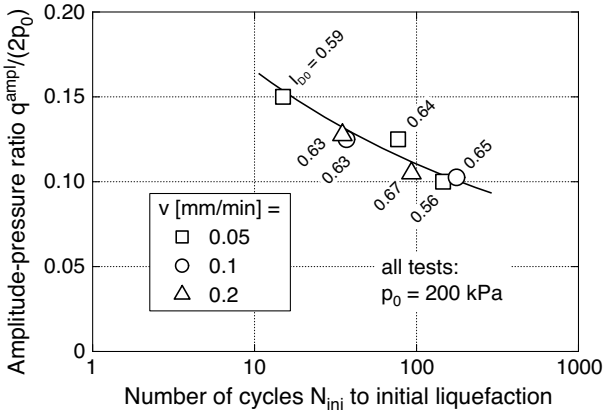


Fig. 17: Amplitude-pressure ratio versus number of cycles to initial liquefaction for different displacement rates applied in the undrained cyclic tests

in good agreement with several other studies documented in the literature (e.g. [30, 45, 58, 64, 65]), which have shown that the liquefaction resistance of sand does not depend on loading frequency.

The effective stress paths and stress-strain curves obtained from simulations of the three tests shown in Figure 12 using hypoplasticity with intergranular strain are presented in Figure 18. The parameters  $R$ ,  $m_R$ ,  $m_T$ ,  $\beta_R$  and  $\chi$  of intergranular strain given in Table 2 have been calibrated based on the data of test TCUI7 performed on medium dense sand (Figure 12c,d). The parameters have been varied until the best possible agreement between the experimental and numerical curves of axial strain amplitude  $\varepsilon_1^{\text{amp}}(N)$  and accumulated pore water pressure  $u^{\text{acc}}(N)$  was achieved, see curves for test TCUI7 in Figure 19. The solid curves in Figure 19 stem from the experiments, while the dashed or dot-dashed ones come out of the simulation with the optimum parameters. Note that a relatively low value of  $m_R = 2.2$  (compared to the recommendation  $m_R = 5$  in [35]) had to be chosen in order to reach a satisfying reproduction of the experimental curves. This is partly due to the relatively high  $h_s$ -value ( $h_s = 4000$  MPa) given in Table 2. With the exception of the first cycle, the parameter  $m_T$  chosen as  $m_R/2$  is rather irrelevant for the simulations of the cyclic triaxial tests since the strain path is always rotated by  $180^\circ$  at the reversals.

It is obvious from Figure 18 that the butterfly-shaped effective stress paths observed during the cyclic mobility phase in the tests on the medium dense and dense samples are not reproduced in the simulations. In contrast to the experiments, the predicted effective stress does not reach  $p = 0$ . After a certain number of cycles the stress paths from the simulations repeatedly pass through an eight-shaped (loose sand) or lens-shaped (medium dense and dense sand) loop. Furthermore, in the simulations the accumulation of axial strain takes place only towards the triaxial extension side (see lower row of diagrams in Figure 18), while the tests show a simultaneous increase of axial strain on both the compression and the extension side within a single cycle.

Figure 19 reveals that the prediction of pore pressure accumulation  $u^{\text{acc}}(N)$  and strain amplitude development  $\varepsilon_1^{\text{amp}}(N)$  for the two tests TCUI1 and TCUI17, performed on loose or dense sand, is less satisfying than in the case

of the test TCUI7 which was the basis for the calibration of the intergranular strain parameters. This demonstrates a known problem: A certain set of intergranular strain parameters can reproduce sufficiently well the elastic strains and the effective stress relaxation in a single test, but usually does not fit well for other test conditions.

#### 4.2 Tests with anisotropic consolidation

Several tests with stress cycles commenced at anisotropic consolidation stresses have been conducted. The testing program is summarized in Table 7. A displacement rate of 0.05 mm/min was used for all tests of this series. Typical results from tests with  $q^{\text{min}} = q_0 - q^{\text{amp}} > 0$  performed on samples with three different densities are shown in Figure 20 (tests TCUA1 - TCUA3). A liquefaction ( $p = 0$ ) is not reached in such tests with  $q^{\text{min}} > 0$ . After a certain number of cycles the accumulated pore water pressure reaches a stable value and thus the effective stress path repeatedly passes through a certain lens-shaped loop, which is located near the failure line known from the undrained monotonic tests. This final stress loop is highlighted by the black colour in the upper row of diagrams in Figure 20 while the rest of the stress path is formatted gray. For a more detailed discussion of the position of the final stress loops with respect to the FL and the PTL the interested reader is referred to [55]. With increasing density of the samples, the overall inclination of the final stress loop increases while its encompassed area in the  $p$ - $q$  plane is reduced. The rate of permanent axial strain accumulation decreases with increasing number of cycles. However, the strain accumulation continues even when the stress relaxation has stopped. The amplitude of axial strain remains almost constant throughout the test [55].

The effective stress paths measured in several tests with anisotropic initial stresses are collected in Figure 21. The tests were performed with different initial densities, consolidation stresses ( $p_0$ ,  $\eta_0 = q_0/p_0$ ) and stress amplitudes. In contrast to the tests shown in Figure 20, a drained first cycle has been applied prior to the undrained cyclic loading in all tests summarized in Figure 21. In [55] the tests shown in Figure 21 have been analyzed regarding the question if the average effective stresses reached after the stabilization of the accumulated pore water pressure are adequately reproduced by the HCA model.

Figure 21 demonstrates that for stress paths completely lying in either the triaxial compression ( $q_{\text{min}} > 0$ ) or extension regime ( $q_{\text{max}} < 0$ ) of the  $p$ - $q$  plane, the final stress loop is lens-shaped. Its inclination in triaxial extension is opposite to that in triaxial compression. The area enclosed by these lenses increases with decreasing values of density and initial stress ratio and with increasing stress amplitude. In case of high densities or large stress amplitudes, the point of maximum deviatoric stress on the final stress loop surpassed the failure line (FL) known from undrained monotonic tests. In contrast, for loose sand or smaller stress amplitudes it has been found lying on or below the FL. If unsymmetrical stress cycles were applied around the  $p$ -axis, i.e. with  $q_0 \neq 0$  and  $q^{\text{amp}} > |q_0|$ , the effective stress path during the last cycles showed a butterfly-like shape (see tests TCUA16 and TCUA17 in Figure 21), i.e.  $p = 0$  was temporarily reached.

The stress-strain curves in all tests with  $q_{\text{min}} > 0$  look similar to those shown in the second row of diagrams in

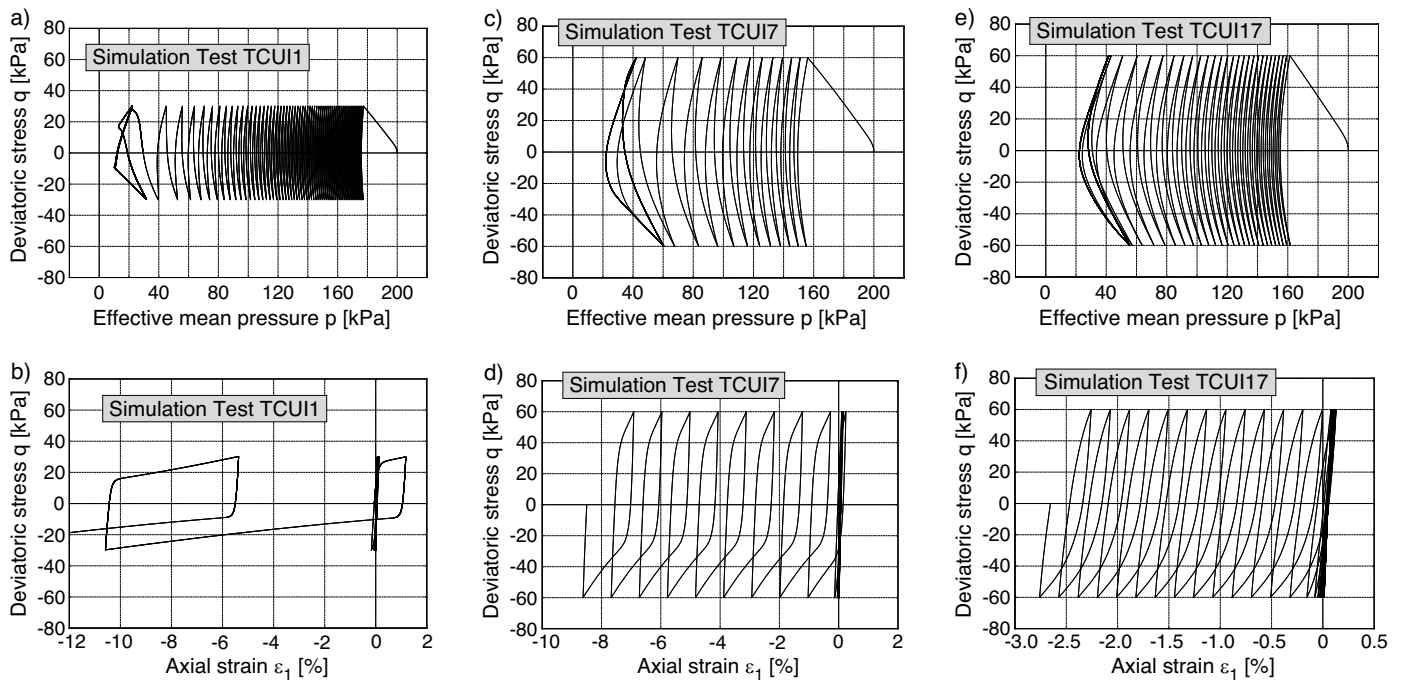


Fig. 18: Simulations of undrained cyclic triaxial tests with isotropic initial stresses and stress cycles using hypoplasticity and intergranular strain: a,b) test TCUI1 ( $I_{D0} = 0.27$ ,  $q^{amp} = 30$  kPa), c,d) test TCUI7 ( $I_{D0} = 0.67$ ,  $q^{amp} = 60$  kPa), e,f) test TCUI17 ( $I_{D0} = 0.87$ ,  $q^{amp} = 60$  kPa)

Test	$e_{0d}$ [-]	$I_{D0d}$ [-]	$e_0$ [-]	$I_{D0}$ [-]	$p_0$ [kPa]	$\eta_0$ [-]	$q^{amp}$ [kPa]	$q^{amp}/p_0$ [-]	1. drained cycle?
TCUA1	-	-	0.945	0.29	300	0.5	120	0.4	no
TCUA2	-	-	0.812	0.64	300	0.5	120	0.4	no
TCUA3	-	-	0.727	0.87	300	0.5	120	0.4	no
TCUA4	0.817	0.63	0.816	0.63	300	0.5	60	0.2	yes
TCUA5	0.820	0.62	0.818	0.63	300	0.5	90	0.3	yes
TCUA6	0.825	0.61	0.823	0.61	300	0.5	120	0.4	yes
TCUA7	0.916	0.37	0.910	0.38	300	0.5	120	0.4	yes
TCUA8	0.732	0.85	0.731	0.86	300	0.5	120	0.4	yes
TCUA9	0.841	0.56	0.840	0.57	100	0.75	25	0.25	yes
TCUA10	0.806	0.66	0.805	0.66	200	0.75	50	0.25	yes
TCUA11	0.819	0.62	0.817	0.63	300	0.75	75	0.25	yes
TCUA12	0.827	0.60	0.826	0.60	200	1.0	60	0.3	yes
TCUA13	0.814	0.64	0.814	0.64	200	0.75	60	0.3	yes
TCUA14	0.840	0.57	0.838	0.57	200	0.5	60	0.3	yes
TCUA15	0.808	0.65	0.807	0.66	200	0.3	60	0.3	yes
TCUA16	0.844	0.56	0.843	0.56	200	0.25	60	0.3	yes
TCUA17	0.810	0.65	0.809	0.65	200	-0.25	60	0.3	yes
TCUA18	0.824	0.61	0.823	0.61	200	-0.25	40	0.2	yes
TCUA19	0.808	0.65	0.804	0.66	200	-0.5	40	0.2	yes

Table 7: Program of undrained cyclic triaxial tests with anisotropic consolidation and stress cycles. Void ratios  $e_0$  and relative densities  $I_{D0}$  measured at initial stress  $p_0$ ,  $\eta_0$  prior to undrained cyclic shearing.  $e_{0d}$  and  $I_{D0d}$  are the values at  $p_0$  prior to the first drained cycle (if applied).

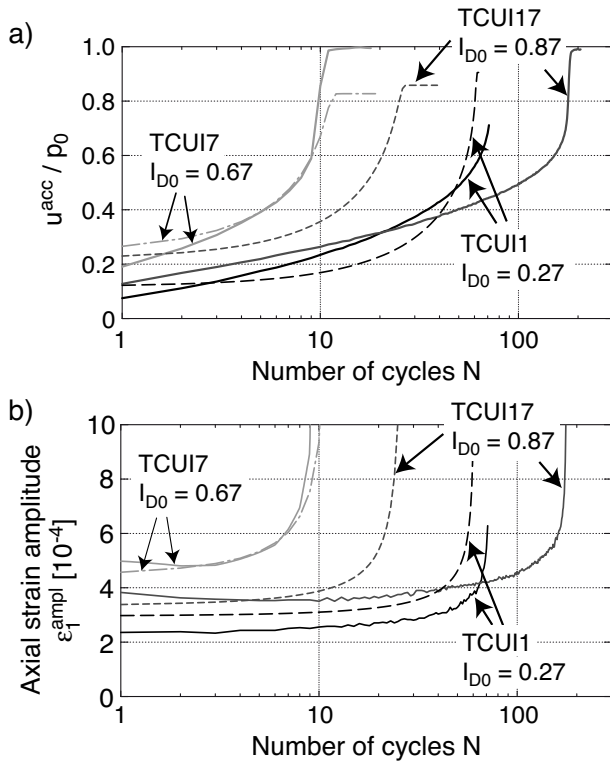


Fig. 19: Comparison of experimentally measured (solid curves) and numerically predicted (dashed or dot-dashed curves) development of accumulated pore water pressure  $u^{acc}(N)$  and axial strain amplitude  $\varepsilon_1^{amp}(N)$  in tests TCUI1, TCUI7 and TCUI17

Figure 20. In case of the unsymmetrical stress cycles applied around the  $p$ -axis (tests TCUA16 and TCUA17), the strain accumulation on the triaxial extension or compression side prevails, depending on whether the main portion of the stress path lies below or above the  $p$ -axis (see Figure 22a,b). The stress-strain relationships in these tests are comparable to those observed for isotropic consolidation stresses (Figure 12d). In case of stress cycles completely applied in the triaxial extension regime of the  $p$ - $q$  plane ( $q_{max} < 0$ ), an accumulation of negative axial strain (extension) takes place (Figure 22c).

The tests results presented in Figures 20 to 22 agree well with the data from several other studies with anisotropic consolidation stresses documented in the literature (e.g. [2, 11, 17, 19, 26, 27, 38–41, 44, 47, 57, 62, 63]). For a more detailed comparison of the present test series with the literature, reference is made to [55].

Curves of pore pressure ratio  $u^{acc}/p_0$  and accumulated strain  $\varepsilon_1^{acc}$  versus the number of cycles are provided in Figure 23. They confirm that the accumulation of residual axial strain continues after the rate of pore pressure accumulation has vanished. The asymptotically reached  $u^{acc}/p_0$  value increases with increasing stress amplitude  $q^{amp}$ , decreasing initial density and decreasing amount of stress ratio  $|\eta_0|$  (Figure 23a,c,e). The rate of residual strain accumulation is larger for higher stress amplitudes, lower relative densities and larger amounts of stress ratio (Figure 23b,d,f).

Simulations with hypoplasticity and intergranular strain of some of the tests with anisotropic initial stresses and stress cycles are presented in Figure 24. The accumula-

tion of compressional axial strain (Figure 24b) and the lens-shaped final stress loop (Figure 24a) in the simulation of test TCUA2 are close to the experimental observations (compare Figure 20c,d). However, when stress relaxation is accomplished, an almost constant rate of strain accumulation  $\varepsilon_1^{acc}$  is obtained in the simulation while the test TCUA2 shows a progressive decay of that rate.

The simulations of tests TCUA16 and TCUA18 include the first drained cycle prior to the undrained cyclic loading. Figure 24 shows the prediction for the undrained phase only. In case of test TCUA16 (Figure 24c,d) with stress cycles slightly exceeding the  $p$ -axis towards the triaxial extension regime, the simulation ends up in a lens-shaped stress path, not reaching  $p = 0$  (similar to the simulations of the tests with isotropic initial stresses in Figure 18). This is in contrast to the test results where the final part of the stress path takes a butterfly-like shape, temporarily passing a state of zero effective stress (Figure 21). The simulation delivers an accumulation of strain towards the compression side only, while the experiment shows a simultaneous increase of strain on both the compression and the extension side (compare Figures 22a and 24d).

In agreement with the corresponding test results (Figure 22c), the simulation of test TCUA18 with cycles completely lying in the triaxial extension regime of the  $p$ - $q$ -plane delivered an accumulation of extensional strain, an inclination of the stress path opposite to the triaxial compression side and a lens-shaped final stress loop (Figure 24e,f). In contrast to the experiments, however, the predicted rate of strain accumulation does not show any decay with increasing number of cycles. Therefore, some aspects of the material response are reproduced by the constitutive model while some others are not.

## 5 Summary and conclusions

The results of oedometric compression tests, drained and undrained monotonic triaxial tests and cyclic undrained triaxial tests on a fine sand have been presented. In the cyclic tests samples of varying density were consolidated isotropically or anisotropically at different values of initial confining pressure  $p_0$  and stress ratio  $\eta_0 = q_0/p_0$ . The stress cycles were applied with different amplitudes  $q^{amp}$ . Together with the results from undrained tests with strain cycles and tests with a combined monotonic and cyclic loading documented in the companion paper [56], this experimental database may serve for the development, calibration and verification of constitutive models with focus to cyclic loading. All test data presented in this paper will be available from [52].

The undrained cyclic triaxial tests with isotropic consolidation and stress cycles showed a butterfly-shaped effective stress path in the final stage (cyclic mobility phase) for medium dense and dense samples. After initial liquefaction ( $p = 0$  is reached for the first time), the axial strain amplitude progressively increased with each subsequent cycle until a certain failure criterion (e.g.  $|\varepsilon_1| = 10\%$ ) was reached. Loose samples failed due to large extensional strains within a single cycle after the effective stress path came near to the failure line in triaxial extension.

When the stress cycles were started at an anisotropic stress ( $q \neq 0$ ) the shape of the final effective stress path and the stress-strain relationship depended on the position of the cycles with respect to the isotropic axis. Similar to the tests with isotropic consolidation, tests with an initial

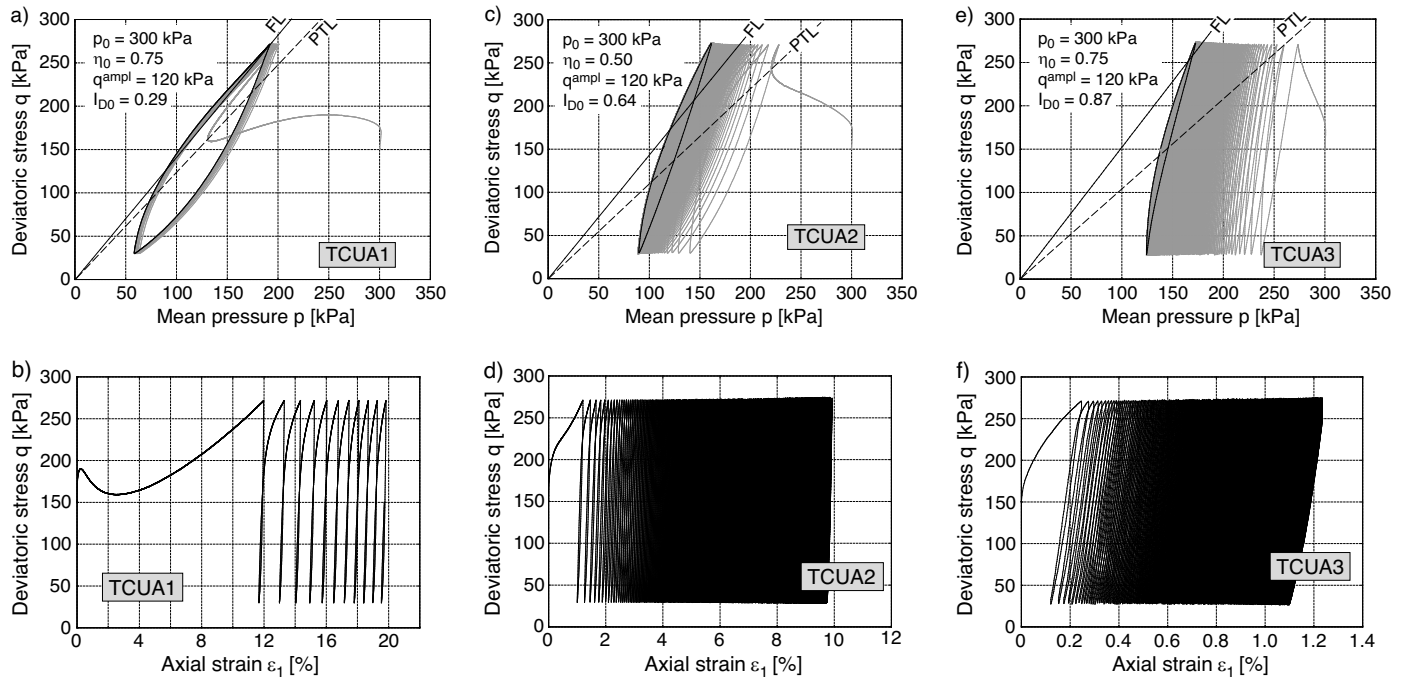


Fig. 20: Results of undrained cyclic triaxial tests with anisotropic initial stresses ( $p_0 = 300$  kPa,  $\eta_0 = 0.5$ ) and stress cycles ( $q^{\text{ampl}} = 120$  kPa), performed without a first drained cycle a,b) test TCUA1 ( $I_{D0} = 0.29$ ), c,d) test TCUA2 ( $I_{D0} = 0.64$ ), e,f) test TCUA3 ( $I_{D0} = 0.87$ )

deviatoric stress  $|q_0| > 0$  and a deviatoric stress amplitude  $q^{\text{ampl}} > |q_0|$  ended up in a butterfly-shaped effective stress path, temporarily passing  $p = 0$ . The accumulation of axial strain on the triaxial extension or compression side prevailed, depending on whether the main portion of the stress path lay below or above the  $p$ -axis.

If the stress cycles did not cross the  $p$ -axis, a zero effective stress ( $p = 0$ ) was not reached. After a certain number of cycles the accumulation of pore water pressure vanished and the effective stress at the end of each subsequent cycle stayed the same. In that phase the effective stress path repeatedly passed through the same lens-shaped loop in the  $p$ - $q$  plane. The area enclosed by this lens was larger for lower densities, lower initial stress ratios and larger stress amplitudes. The tests showed that the maximum deviatoric stress on the final stress loop can significantly exceed the failure line derived from the undrained monotonic tests, if the stress amplitude is large and the density is high. In contrast, for smaller stress amplitudes or lower densities, this point was observed to lie on or even below the FL. The effective stress paths during cycles fully applied in the triaxial extension regime ( $q_{\text{max}} < 0$ ) showed an opposite inclination to those observed for triaxial compression ( $q_{\text{min}} > 0$ ). An accumulation of compressional axial strain took place in tests with  $q_{\text{min}} > 0$ , while extensional strains cumulated in tests with  $q_{\text{max}} < 0$ . The strain accumulation continued even when the accumulated pore water pressure had become stable, i.e. when stress relaxation was terminated. The rate of this strain accumulation decayed with increasing number of cycles.

As an example for the examination of an existing constitutive model based on the presented experimental data, selected tests have been recalculated using hypoplasticity with intergranular strain. The simulations demonstrate

that some parts of the material response can be reproduced well (e.g. stress strain curves in monotonic tests, lens-shaped final stress loops in cyclic tests with anisotropic consolidation) while some other experimental observations are not captured satisfactory (e.g. no stress relaxation to  $p = 0$  and no butterfly-shaped effective stress loops for tests with isotropic consolidation, accumulation of strain to the extension side only in tests with  $q_0 = 0$ , pore pressure accumulation curves  $u^{\text{acc}}(N)$  fit for one test but show large deviations from the experimental data for tests with other boundary conditions). The simulations demonstrate the difficulty of reproducing all different kinds of test conditions by a single constitutive model with a limited number of parameters. They highlight the need for further improvements of the existing models or for novel models that deliver a better description of the experimental results. Each reader is encouraged to check his own constitutive model against the data base published herein.

### Acknowledgement

Parts of the presented study have been performed within the framework of the project "Geotechnical robustness and self-healing of foundations of offshore wind power plants" funded by the German Federal Ministry for the Environment, Nature Conservation and Nuclear Safety (BMU, project No. 0327618). Other parts were conducted within the framework of the project "Improvement of an accumulation model for high-cyclic loading" funded by German Research Council (DFG, project No. TR218/18-1 / WI3180/3-1). The authors are grateful to BMU and DFG for the financial support. All tests have been performed by the technicians H. Borowski, P. Gözl and N. Demiral in the IBF soil mechanics laboratory.

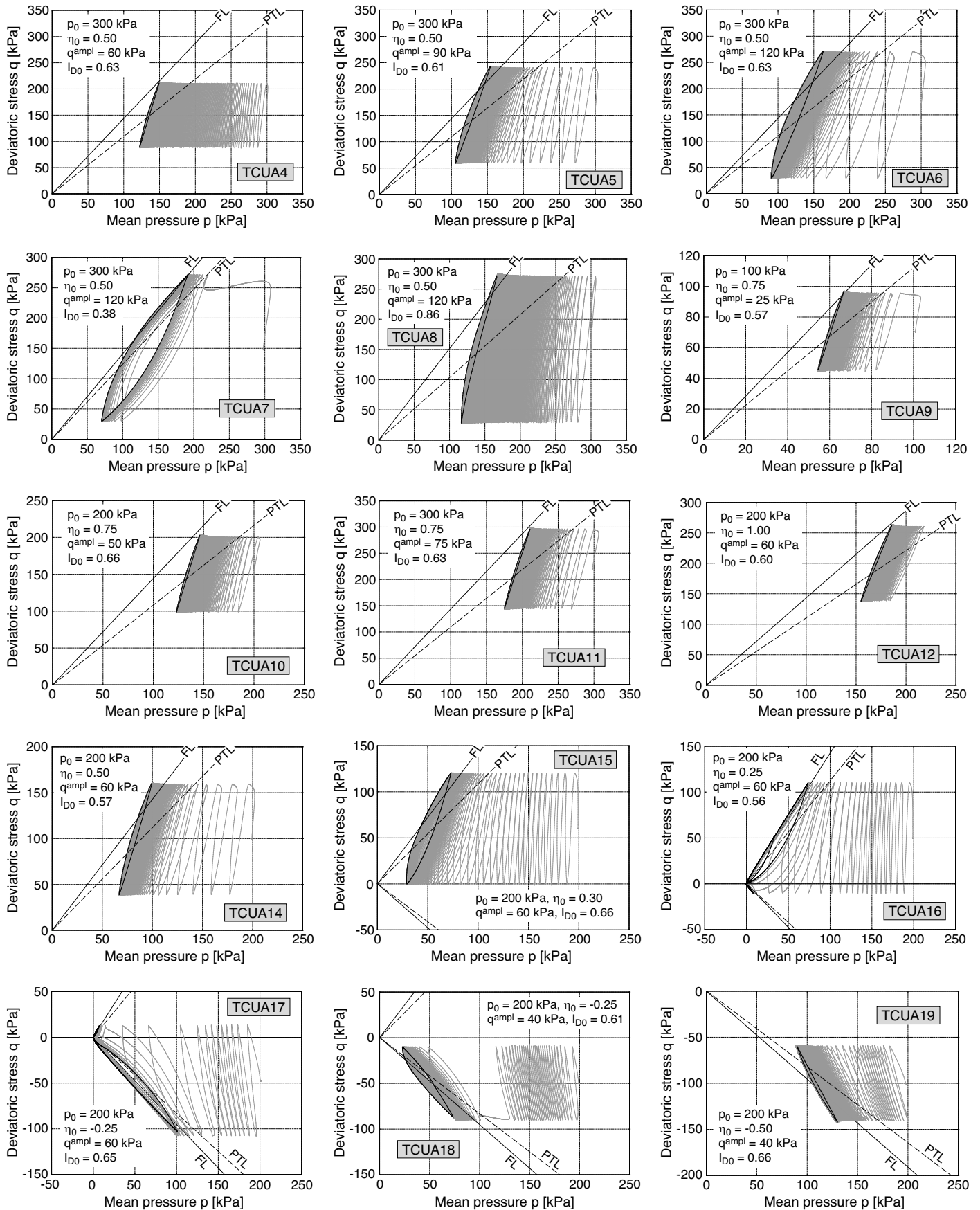


Fig. 21: Effective stress paths measured in undrained cyclic triaxial tests with anisotropic consolidation and stress cycles. The values of  $p_0$ ,  $\eta_0$ ,  $I_{D0}$  and  $q^{ampl}$  have been varied from test to test.

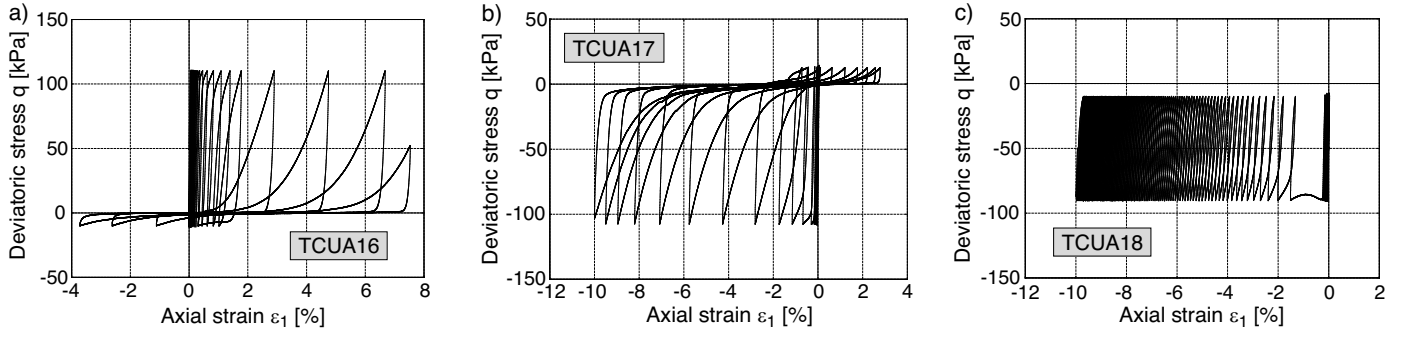
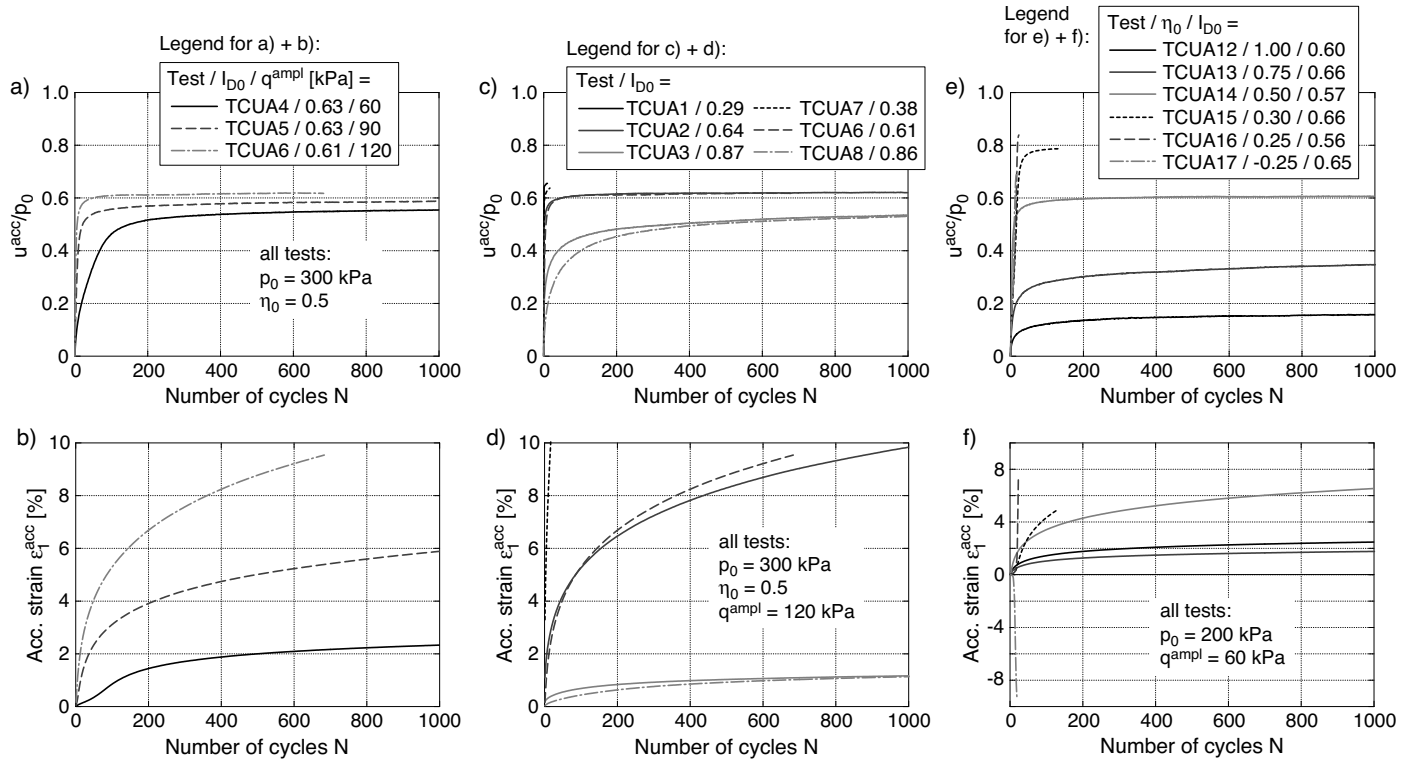


Fig. 22: Stress-strain curves in the tests TCUA16, TCUA17 and TCUA18


 Fig. 23: Ratio of accumulated pore water pressure  $u^{\text{acc}}$  and initial mean effective stress  $p_0$  as a function of the number of cycles measured in undrained cyclic triaxial tests with anisotropic consolidation stresses and different a,b) stress amplitudes  $q^{\text{ampl}}$ , c,d) initial densities  $I_{D0}$  and e,f) initial stress ratios  $\eta_0$ 

## A Equations of the constitutive model used for the element test simulations

### A.1 Notation

Scalar variables are denoted by characters with normal letters (e.g.  $e$ ), second-order tensors are formatted fat (e.g.  $\boldsymbol{\sigma}$ ,  $\mathbf{h}$ ), while fourth-order tensors are given in sans-serif font (e.g.  $\mathbf{L}$ ,  $\mathbf{I}$ ). A dyadic product is denoted by  $\mathbf{a} \otimes \mathbf{b}$  (i.e.  $a_{ij} b_{kl}$  in index notation), a single contraction by  $\mathbf{a} \cdot \mathbf{b} \hat{=} a_{ik} b_{kj}$  and a double contraction by  $\mathbf{a} : \mathbf{b} \hat{=} a_{kl} b_{kl}$ . The Euclidean norm is defined as  $\|\mathbf{a}\| = \sqrt{\mathbf{a} : \mathbf{a}}$ , the trace of a tensor as  $\text{tr}(\mathbf{a}) \hat{=} a_{kk}$  and the deviator as  $\mathbf{a}^* = \mathbf{a} - \text{tr}(\mathbf{a})/3 \mathbf{1}$  with the second-order identity tensor  $\mathbf{1} \hat{=} \delta_{ij}$ . The Kronecker symbol  $\delta_{ij}$  is equal to 1 for  $i = j$  and 0 for  $i \neq j$ . A normalization is denoted by an arrow above the respective symbol  $\vec{\mathbf{a}} = \mathbf{a}/\|\mathbf{a}\|$  and a division by the trace of the tensor is identified by a roof  $\hat{\mathbf{a}} = \mathbf{a}/\text{tr}(\mathbf{a})$ .

### A.2 Basic hypoplastic model after von Wolffersdorff [51]

The basic equation of the hypoplastic model proposed by von Wolffersdorff [51] reads:

$$\dot{\boldsymbol{\sigma}} = \mathbf{L} : \dot{\boldsymbol{\varepsilon}} + \mathbf{N} \|\dot{\boldsymbol{\varepsilon}}\| = \underbrace{\left( \mathbf{L} + \mathbf{N} \frac{\dot{\boldsymbol{\varepsilon}}}{\|\dot{\boldsymbol{\varepsilon}}\|} \right)}_{\mathbf{M}} : \dot{\boldsymbol{\varepsilon}} \quad (7)$$

with Jaumann stress rate  $\dot{\boldsymbol{\sigma}}$ , strain rate  $\dot{\boldsymbol{\varepsilon}}$  and the linear and nonlinear stiffness tensors  $\mathbf{L}$  and  $\mathbf{N}$ :

$$\mathbf{L} = f_b f_e \frac{1}{\dot{\boldsymbol{\sigma}} : \dot{\boldsymbol{\sigma}}} (F^2 \mathbf{I} + a^2 \dot{\boldsymbol{\sigma}} \otimes \dot{\boldsymbol{\sigma}}) \quad (8)$$

$$\mathbf{N} = f_b f_e f_d \frac{F a}{\dot{\boldsymbol{\sigma}} : \dot{\boldsymbol{\sigma}}} (\dot{\boldsymbol{\sigma}} + \dot{\boldsymbol{\sigma}}^*) \quad (9)$$

Therein  $I_{ijkl} = 0.5(\delta_{ik}\delta_{jl} + \delta_{il}\delta_{jk})$  is a fourth-order identity tensor. The parameters  $a$  and  $F$  in Equations (8) and (9)

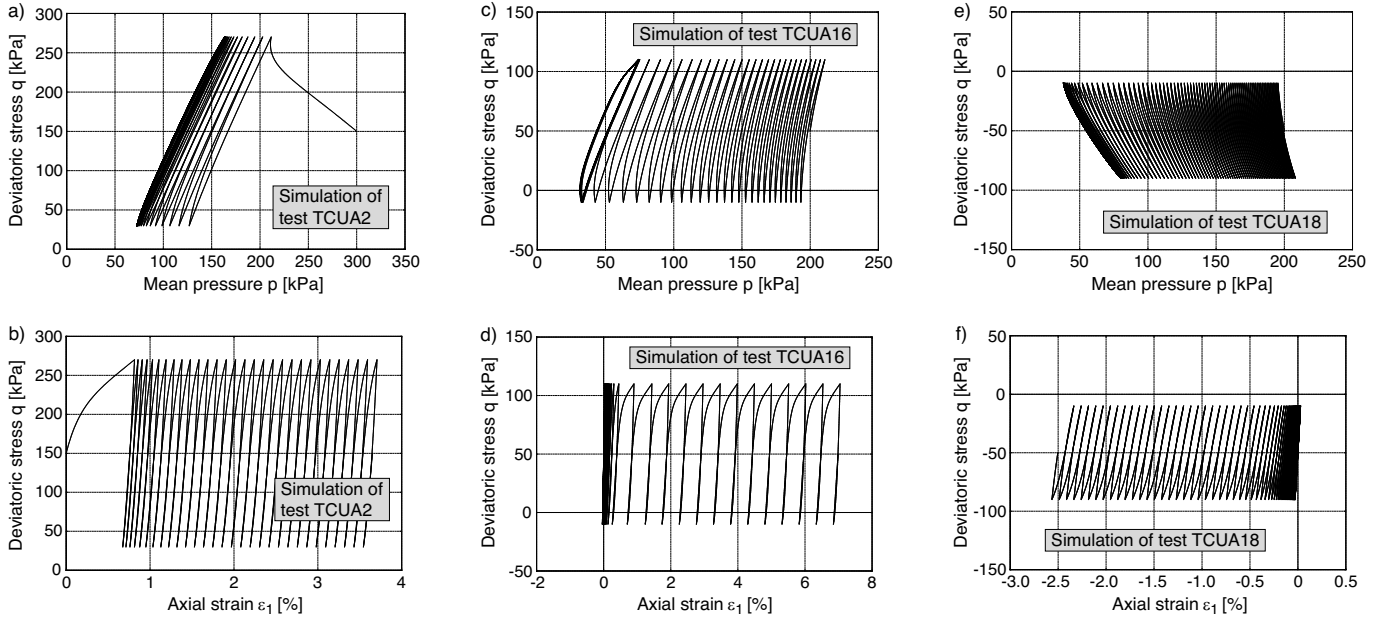


Fig. 24: Simulations with hypoplasticity and intergranular strain of undrained cyclic tests with anisotropic initial stresses and stress cycles: a,b) test TCUA2 ( $I_{D0} = 0.64$ ,  $p_0 = 300$  kPa,  $\eta_0 = 0.5$ ,  $q^{\text{ampl}} = 120$  kPa), c,d) test TCUA16 ( $I_{D0} = 0.56$ ,  $p_0 = 200$  kPa,  $\eta_0 = 0.25$ ,  $q^{\text{ampl}} = 60$  kPa), e,f) test TCUA18 ( $I_{D0} = 0.61$ ,  $p_0 = 200$  kPa,  $\eta_0 = -0.25$ ,  $q^{\text{ampl}} = 40$  kPa)

describe the failure criterion of Matusoka & Nakai [32]:

$$a = \frac{\sqrt{3} (3 - \sin \varphi_c)}{2 \sqrt{2} \sin \varphi_c} \quad (10)$$

$$F = \sqrt{\frac{1}{8} \tan^2 \psi + \frac{2 - \tan^2 \psi}{2 + \sqrt{2} \tan \psi \cos(3\theta)}} - \frac{\tan \psi}{2 \sqrt{2}} \quad (11)$$

$$\tan \psi = \sqrt{3} \|\hat{\sigma}^*\| \quad (12)$$

$$\cos(3\theta) = -\sqrt{6} \frac{\text{tr}(\hat{\sigma}^* \cdot \hat{\sigma}^* \cdot \hat{\sigma}^*)}{[\hat{\sigma}^* : \hat{\sigma}^*]^{\frac{3}{2}}} \quad (13)$$

$\varphi_c$  is the critical friction angle (material constant). The barotropy and pyknotropy factors read:

$$f_d = \left( \frac{e - e_d}{e_c - e_d} \right)^\alpha \quad (14)$$

$$f_e = \left( \frac{e_c}{e} \right)^\beta \quad (15)$$

$$f_b = \frac{\left( \frac{e_{i0}}{e_{c0}} \right)^\beta \frac{h_s}{n} \frac{1+e_i}{e_i} \left( \frac{3p}{h_s} \right)^{1-n}}{3 + a^2 - a \sqrt{3} \left( \frac{e_{i0} - e_{d0}}{e_{c0} - e_{d0}} \right)^\alpha} \quad (16)$$

with material constants  $\alpha$ ,  $\beta$ ,  $h_s$  and  $n$ . The pressure-dependence of the void ratios  $e_d$ ,  $e_c$  and  $e_i$ , corresponding to the densest, the critical and the loosest possible state is described by (Bauer [5]):

$$\frac{e_i}{e_{i0}} = \frac{e_c}{e_{c0}} = \frac{e_d}{e_{d0}} = \exp \left[ - \left( \frac{3p}{h_s} \right)^n \right] \quad (17)$$

with the void ratios  $e_{i0}$ ,  $e_{c0}$  and  $e_{d0}$  (material constants) at pressure  $p = 0$ . The material parameters  $e_{i0}$ ,  $e_{c0}$ ,  $e_{d0}$ ,  $\varphi_c$ ,  $h_s$ ,  $n$ ,  $\alpha$  and  $\beta$  used for the simulations are summarized in the first eight columns of Table 2.

### A.3 Extension of hypoplastic model by intergranular strain according to Niemunis & Herle [35]

In order to eliminate an excessive accumulation of strain (ratcheting) of the original hypoplastic model proposed by von Wolfersdorff [51] in the case of a cyclic loading, Niemunis & Herle [35] introduced the additional state variable "intergranular strain"  $\mathbf{h}$ , which memorizes the last part of the previous strain path. A measure of the mobilization of the intergranular strain is  $\rho = \|\mathbf{h}\|/R$  with a material constant  $R$  describing the range of an elastic locus. Depending on the actual strain rate  $\dot{\epsilon}$  in relation to the direction of the intergranular strain  $\mathbf{h}$ , the stiffness  $M$  in Equation (7) is increased according to:

$$M = [\rho^\chi m_T + (1 - \rho^\chi) m_R] L + \begin{cases} \rho^\chi (1 - m_T) L : \vec{\mathbf{h}} \otimes \vec{\mathbf{h}} + \rho^\chi \mathbf{N} \otimes \vec{\mathbf{h}} & \text{for } \vec{\mathbf{h}} : \dot{\epsilon} > 0 \\ \rho^\chi (m_R - m_T) L : \vec{\mathbf{h}} \otimes \vec{\mathbf{h}} & \text{for } \vec{\mathbf{h}} : \dot{\epsilon} \leq 0 \end{cases} \quad (18)$$

with material constants  $m_T$ ,  $m_R$  and  $\chi$ . The evolution of the rate  $\dot{\mathbf{h}}$  of intergranular strain obeys:

$$\dot{\mathbf{h}} = \begin{cases} (1 - \vec{\mathbf{h}} \otimes \vec{\mathbf{h}} \varrho^{\beta_r}) : \dot{\epsilon} & \text{for } \vec{\mathbf{h}} : \dot{\epsilon} > 0 \\ \dot{\epsilon} & \text{for } \vec{\mathbf{h}} : \dot{\epsilon} \leq 0 \end{cases} \quad (19)$$

with another material constant  $\beta_r$ . If a sufficiently large monotonic strain is applied after a change of the strain

path direction, the comparatively low stiffness of the original hypoplastic model according to Eq. (7) is regained. The material parameters  $R$ ,  $m_T$ ,  $m_R$ ,  $\chi$  and  $\beta_r$ , used for the simulations are summarized in the last five columns of Table 2.

## References

- [1] DIN 18126: Bestimmung der Dichte nichtbindiger Böden bei lockerster und dichtester Lagerung, 1996.
- [2] G. Arangelovski and I. Towhata. Accumulated deformation of sand with initial shear stress and effective stress state lying near failure conditions. *Soils and Foundations*, 44(6):1–16, 2004.
- [3] A. L. Baki, M. M. Rahman, S. R. Lo, and C. T. Gnanendran. Linkage between static and cyclic liquefaction of loose sand with a range of fines contents. *Canadian Geotechnical Journal*, 49:891–906, 2012.
- [4] M. A. L. Baki, M. M. Rahman, and S. R. Lo. Predicting onset of cyclic instability of loose sand with fines using instability curves. *Soil Dynamics and Earthquake Engineering*, 61-62(3):140–151, 2014.
- [5] E. Bauer. Calibration of a comprehensive constitutive equation for granular materials. *Soils and Foundations*, 36:13–26, 1996.
- [6] K. Been and M.G. Jefferies. A state parameter for sands. *Géotechnique*, 35(1):99–112, 1985.
- [7] A.W. Bishop and G.E. Green. The influence of end restraint on the compression strength of a cohesionless soil. *Géotechnique*, 15(3):243–266, 1965.
- [8] G.D. Bouckovalas, K.I. Andrianopoulos, and A.G. Papadimitriou. A critical state interpretation for the cyclic liquefaction of silty sands. *Soil Dynamics and Earthquake Engineering*, 23:115–125, 2003.
- [9] R.W. Boulanger. High overburden stress effects in liquefaction analyses. *Journal of Geotechnical and Geoenvironmental Engineering, ASCE*, 129(12):1071–1082, 2003.
- [10] Y.C. Chen and T.S. Liao. Studies of the state parameter and liquefaction resistance of sand. In *Proceedings of the 2nd International Conference on Earthquake Geotechnical Engineering, Lisbon, Portugal*, pages 513–518, 1999.
- [11] G. Chiaro, J. Koseki, and T. Sato. Effects of initial static shear on liquefaction and large deformation properties of loose saturated Toyoura sand in undrained cyclic torsional shear tests. *Soils and Foundations*, 52(3):498–510, 2012.
- [12] Y. Dafalias and M. Manzari. Simple plasticity sand model accounting for fabric change effects. *Journal of Engineering Mechanics*, 130(6):622–634, 2004.
- [13] Y. Dafalias, A. Papadimitriou, and X. Li. Sand plasticity model accounting for inherent fabric anisotropy. *Journal of Engineering Mechanics*, 130(11):1319–1333, 2004.
- [14] H.K. Dash, T.G. Sitharam, and B.A. Baudet. Influence of non-plastic fines on the response of a silty sand to cyclic loading. *Soils and Foundations*, 50(5):695–704, 2010.
- [15] A. Flora, S. Lirer, and F. Silvestri. Undrained cyclic resistance of undisturbed gravelly soils. *Soil Dynamics and Earthquake Engineering*, 43:366–379, 2012.
- [16] W. Fuentes. Contributions in mechanical modelling of fill material. Dissertation, Veröffentlichungen des Institutes für Bodenmechanik und Felsmechanik am Karlsruher Institut für Technologie, Heft 179, 2014.
- [17] V.N. Georgiannou and M. Konstadinou. Effects of density on cyclic behaviour of anisotropically consolidated Ottawa sand under undrained torsional loading. *Géotechnique*, 64(4):287–302, 2014.
- [18] V.N. Georgiannou and A. Tsomokos. Comparison of two fine sands under torsional loading. *Canadian Geotechnical Journal*, 45:1659–1672, 2008.
- [19] V.N. Ghionna and D. Porcino. Liquefaction resistance of undisturbed and reconstituted samples of a natural coarse sand from undrained triaxial tests. *Journal of Geotechnical and Geoenvironmental Engineering, ASCE*, 132(2):194–201, 2006.
- [20] M. Hatanaka, L. Feng, N. Matsumura, and H. Yasu. A study on the engineering properties of sand improved by the sand compaction pile method. *Soils and Foundations*, 48(1):73–85, 2008.
- [21] M. Hatanaka, A. Uchida, and J. Ohara. Liquefaction characteristics of a gravelly fill liquefied during the 1995 Hyogo-Ken Nanbu earthquake. *Soils and Foundations*, 37(3):107–115, 1997.
- [22] I. Herle. Hypoplastizität und Granulometrie einfacher Korngerüste. Dissertation, Institut für Bodenmechanik und Felsmechanik der Universität Fridericiana in Karlsruhe, Heft Nr. 142, 1997.
- [23] A.-B. Huang and S.-Y. Chuang. Correlating cyclic strength with fines contents through state parameters. *Soils and Foundations*, 51(6):991–1001, 2011.
- [24] M. Hyodo, A.F.L. Hyde, and N. Aramaki. Liquefaction of crushable soils. *Géotechnique*, 48(4):527–543, 1998.
- [25] M. Hyodo, A.F.L. Hyde, N. Aramaki, and Y. Nakata. Undrained monotonic and cyclic shear behaviour of sand under low and high confining stresses. *Soils and Foundations*, 42(3):63–76, 2002.
- [26] M. Hyodo, H. Murata, N. Yasufuku, and T. Fujii. Undrained cyclic shear strength and residual shear strain of saturated sand by cyclic triaxial tests. *Soils and Foundations*, 31(3):60–76, 1991.
- [27] M. Hyodo, H. Tanimizu, N. Yasufuku, and H. Murata. Undrained cyclic and monotonic triaxial behaviour of saturated loose sand. *Soils and Foundations*, 34(1):19–32, 1994.
- [28] T. Kiyota, J. Koseki, and T. Sato. Relationship between limiting shear strain and reduction of shear moduli due to liquefaction in large strain torsional shear tests. *Soil Dynamics and Earthquake Engineering*, 49:122–134, 2013.
- [29] T. Kiyota, T. Sato, J. Koseki, and M. Abadimarand. Behavior of liquefied sands under extremely large strain levels in cyclic torsional shear tests. *Soils and Foundations*, 48(5):727–739, 2008.
- [30] T. Kokusho, T. Hara, and R. Hiraoka. Undrained shear strength of granular soils with different particle gradations. *Journal of Geotechnical and Geoenvironmental Engineering, ASCE*, 130(6):621–629, 2004.
- [31] M. Konstadinou and V.N. Georgiannou. Cyclic behaviour of loose anisotropically consolidated Ottawa sand under undrained torsional loading. *Géotechnique*, 63(13):1144–1158, 2013.
- [32] H. Matsuoka and T. Nakai. A new failure criterion for soils in three-dimensional stresses. In *Deformation and Failure of Granular Materials*, pages 253–263, 1982. Proc. IUTAM Symp. in Delft.
- [33] A. Niemunis. Extended hypoplastic models for soils. Habilitation, Veröffentlichungen des Institutes für Grundbau und Bodenmechanik, Ruhr-Universität Bochum, Heft Nr. 34, 2003. available from [www.pg.gda.pl/~aniem/an-liter.html](http://www.pg.gda.pl/~aniem/an-liter.html).
- [34] A. Niemunis. Incremental Driver User’s manual. , 2008. available from [www.pg.gda.pl/~aniem/an-liter.html](http://www.pg.gda.pl/~aniem/an-liter.html).

- [35] A. Niemunis and I. Herle. Hypoplastic model for cohesionless soils with elastic strain range. *Mechanics of Cohesive-Frictional Materials*, 2(4):279–299, 1997.
- [36] A. Niemunis, T. Wichtmann, and Th. Triantafyllidis. A high-cycle accumulation model for sand. *Computers and Geotechnics*, 32(4):245–263, 2005.
- [37] M. Oda, K. Kawamoto, K. Suzuki, H. Fujimori, and M. Sato. Microstructural interpretation on reliquefaction of saturated granular soils under cyclic loading. *Journal of Geotechnical and Geoenvironmental Engineering, ASCE*, 127(5):416–423, 2001.
- [38] F. Oka, A. Yashima, A. Tateishi, Y. Taguchi, and S. Yamashita. A cyclic elasto-plastic constitutive model for sand considering a plastic-strain dependence of the shear modulus. *Géotechnique*, 49(5):661–680, 1999.
- [39] D. Porcino, G. Caridi, and V.N. Ghionna. Undrained monotonic and cyclic simple shear behaviour of carbonate sand. *Géotechnique*, 58(8):635–644, 2008.
- [40] S.S. Sharma and M. Ismail. Monotonic and cyclic behavior of two calcareous soils of different origins. *Journal of Geotechnical and Geoenvironmental Engineering, ASCE*, 132(12):1581–1591, 2006.
- [41] S. Sivathayalan and D. Ha. Effect of static shear stress on the cyclic resistance of sands in simple shear loading. *Canadian Geotechnical Journal*, 48:1471–1484, 2011.
- [42] C. A. Stamatopoulos. An experimental study of the liquefaction strength of silty sands in terms of the state parameter. *Soil Dynamics and Earthquake Engineering*, 30(2):662–678, 2010.
- [43] C.A. Stamatopoulos, A.C. Stamatopoulos, and L.N. Balla. Cyclic strength of sands in terms of the state parameter. In *The 11th International Conference on Soil Dynamics and Earthquake Engineering (11th ICSD) and the 3rd International Conference on Geotechnical Earthquake Engineering*, 2004.
- [44] H.Y. Sze and J. Yang. Failure modes of sand in undrained cyclic loading: Impact of sample preparation. *Journal of Geotechnical and Geoenvironmental Engineering, ASCE*, 140(1):152–169, 2014.
- [45] F. Tatsuoka, S. Maeda, K. Ochi, and S. Fujii. Prediction of cyclic undrained strength of sand subjected to irregular loadings. *Soils and Foundations*, 26(2):73–89, 1986.
- [46] F. Tatsuoka, S. Toki, S. Miura, H. Kato, M. Okamoto, S.-I. Yamada, S. Yasuda, and F. Tanizawa. Some factors affecting cyclic undrained triaxial strength of sand. *Soils and Foundations*, 26(3):99–116, 1986.
- [47] Y.P. Vaid and J.C. Chern. Effect of static shear on resistance to liquefaction. *Soils and Foundations*, 28(1):47–60, 1983.
- [48] Y.P. Vaid, E.K.F. Chung, and R.H. Kuerbis. Preshearing and undrained response of sands. *Soils and Foundations*, 29(4):49–61, 1989.
- [49] Y.P. Vaid and S. Sivathayalan. Fundamental factors affecting liquefaction susceptibility of sands. *Canadian Geotechnical Journal*, 37:592–606, 2000.
- [50] R. Verdugo and K. Ishihara. The steady state of sandy soils. *Soils and Foundations*, 36(2):81–91, 1996.
- [51] P.-A. von Wolffersdorff. A hypoplastic relation for granular materials with a predefined limit state surface. *Mechanics of Cohesive-Frictional Materials*, 1(3):251–271, 1996.
- [52] T. Wichtmann. [www.torsten-wichtmann.de](http://www.torsten-wichtmann.de). Homepage, 2018.
- [53] T. Wichtmann, A. Niemunis, and Th. Triantafyllidis. On the "elastic stiffness" in a high-cycle accumulation model - continued investigations. *Canadian Geotechnical Journal*, 50(12):1260–1272, 2013.
- [54] T. Wichtmann, A. Niemunis, Th. Triantafyllidis, and M. Poblete. Correlation of cyclic preloading with the liquefaction resistance. *Soil Dynamics and Earthquake Engineering*, 25(12):923–932, 2005.
- [55] T. Wichtmann and Th. Triantafyllidis. Stress attractors predicted by a high-cycle accumulation model confirmed by undrained cyclic triaxial tests. *Soil Dynamics and Earthquake Engineering*, 69(2):125–137, 2014.
- [56] T. Wichtmann and Th. Triantafyllidis. An experimental data base for the development, calibration and verification of constitutive models for sand with focus to cyclic loading. Part II: tests with strain cycles and combined cyclic and monotonic loading. *Acta Geotechnica*, 11(4):763–774, 2016.
- [57] D. Wijewickreme, S. Sriskandakumar, and P. Byrne. Cyclic loading response of loose air-pluviated Fraser River sand for validation of numerical models simulating centrifuge tests. *Canadian Geotechnical Journal*, 42:550–561, 2005.
- [58] R.T. Wong, H.B. Seed, and C.K. Chan. Cyclic loading liquefaction of gravelly soils. *Journal of the Geotechnical Engineering Division, ASCE*, 101(GT6):571–583, 1975.
- [59] V.C. Xenaki and G.A. Athanasopoulos. Liquefaction resistance of sand - silt mixtures: an experimental investigation of the effects of fines. *Soil Dynamics and Earthquake Engineering*, 23:183–194, 2003.
- [60] S. Yamada, T. Takamori, and K. Sato. Effects on reliquefaction resistance produced by changes in anisotropy during liquefaction. *Soils and Foundations*, 50(1):9–25, 2010.
- [61] S. Yamashita and S. Toki. Effects of fabric anisotropy of sand on cyclic undrained triaxial and torsional strengths. *Soils and Foundations*, 33(3):92–104, 1993.
- [62] J. Yang and H.Y. Sze. Cyclic behaviour and resistance of saturated sand under non-symmetrical loading conditions. *Géotechnique*, 61(1):59–73, 2011.
- [63] J. Yang and H.Y. Sze. Cyclic strength of sand under sustained shear stress. *Journal of Geotechnical and Geoenvironmental Engineering, ASCE*, 137(12):1275–1285, 2011.
- [64] S. Yasuda and M. Soga. Effects of frequency on undrained strength of sands (in Japanese). In *Proc. 19th Nat. Conf. Soil Mech. Found. Eng.*, pages 549–550, 1984.
- [65] Y. Yoshimi and H. Oh-Oka. Influence of degree of shear stress reversal on the liquefaction potential of saturated sand. *Soils and Foundations*, 15(3):27–40, 1975.
- [66] J.-M. Zhang, Y. Shamoto, and K. Tokimatsu. Moving critical and phase-transformation stress state lines of saturated sand during undrained cyclic shear. *Soils and Foundations*, 37(2):51–59, 1997.
- [67] J.-M. Zhang and G. Wang. Large post-liquefaction deformation of sand, part I: physical mechanism, constitutive description and numerical algorithm. *Acta Geotechnica*, 7:69–113, 2012.